AGU PUBLICATIONS

Water Resources Research

RESEARCH ARTICLE

10.1002/2017WR020883

Key Points:
- Direct measurements of lift and drag forces were made on cobbles in steep flume experiments with shallow, rough flow over a planar bed
- As flows shallow, drag coefficients increase, turbulent fluctuations decrease, and lift forces are negative, pulling particles to the bed
- Results help explain high flow resistance, high critical Shields numbers, and low sediment transport rates in mountain streams

Supporting Information:
- Supporting Information S1

Correspondence to:
M. P. Lamb,
mpl@gps.caltech.edu

Citation:
Lamb, M. P., and F. Brun (2017), Direct measurements of lift and drag on shallowly submerged cobbles in steep streams: Implications for flow resistance and sediment transport, *Water Resour. Res.*, *53*, doi:10.1002/2017WR020883.

Received 4 APR 2017
Accepted 6 AUG 2017
Accepted article online 18 AUG 2017

Direct measurements of lift and drag on shallowly submerged cobbles in steep streams: Implications for flow resistance and sediment transport

Michael P. Lamb[1], Fanny Brun[1], and Brian M. Fuller[1]

[1]Division of Geological and Planetary Sciences, California Institute of Technology, Pasadena, California, USA

Abstract Steep mountain streams have higher resistance to flow and lower sediment transport rates than expected by comparison with low gradient rivers, and often these differences are attributed to reduced near-bed flow velocities and stresses associated with form drag on channel forms and immobile boulders. However, few studies have directly measured drag and lift forces acting on bed sediment for shallow flows over coarse sediment, which ultimately control sediment transport rates and grain-scale flow resistance. Here we report on particle lift and drag force measurements in flume experiments using a planar, fixed cobble bed over a wide range of channel slopes ($0.004 < S < 0.3$) and water discharges. Drag coefficients are similar to previous findings for submerged particles ($C_D \sim 0.7$) but increase significantly for partially submerged particles. In contrast, lift coefficients decrease from near unity to zero as the flow shallows and are strongly negative for partially submerged particles, indicating a downward force that pulls particles toward the bed. Fluctuating forces in lift and drag decrease with increasing relative roughness, and they scale with the depth-averaged velocity squared rather than the bed shear stress. We find that, even in the absence of complex bed topography, shallow flows over coarse sediment are characterized by high flow resistance because of grain drag within a roughness layer that occupies a significant fraction of the total flow depth, and by heightened critical Shields numbers and reduced sediment fluxes because of reduced lift forces and reduced turbulent fluctuations.

Plain Language Abstract Steep mountain streams have slower flow and they transport less sediment as compared to lower gradient rivers. Often these observations are attributed to complex river-bed geometries, but little work has explored steep rivers with simple, flat riverbeds. To address this gap in observations, we performed a series of experiments in a controlled indoor river facility and measured directly the forces that flowing water imparts on streambed cobbles and boulders. Under the shallow, rough water flows common to mountain streams, we found that downstream oriented drag forces significantly increase in shallow flow. On the contrary, vertically oriented forces pull the cobbles towards the river bed, rather than the more common scenario where they lift sediment off the bed. We also observed a lower intensity of turbulence in steep rivers, despite the vigorous appearance of the water. Combined, these observations help to explain reduced water flow and sediment transport rates in mountain rivers.

1. Motivation

Mountain streams convey to lower gradient rivers water, organic and inorganic sediment, and a suite of solutes and nutrients, and predicting their fluxes is important for a broad range of topics including flood hazard mitigation, habitat restoration, landscape evolution, and biogeochemical cycling [*Buffington et al.*, 2004; *Bernhardt et al.*, 2005; *Rickenmann*, 2012; *Scheingross et al.*, 2013]. The hydrodynamics and sediment transport processes in mountain streams are poorly understood and they differ from better studied lower gradient rivers (e.g., with bed slopes, $S < 1\%$). For example, the friction coefficient, C_f, which relates the depth-averaged surface flow velocity, U_{surf}, to bed shear stress (i.e., $C_f = u_*^2/U_{surf}^2$ where $u_* = \sqrt{\tau_b/\rho_w}$ is the bed shear velocity, τ_b is the bed shear stress, and ρ_w is water density), is large in mountain streams and can deviate strongly from relations developed for lower gradient rivers [*Bathurst*, 1985, 2002; *Aberle and Smart*, 2003; *Ferro*, 2003; *Wilcox et al.*, 2006; *Ferguson*, 2007; *Rickenmann and Recking*, 2011]. Moreover, sediment transport relations developed for lowland rivers typically underpredict the bed shear stress necessary to initiate

sediment transport by as much as a factor of 5 [*Mueller et al*., 2005; *Lamb et al*., 2008; *Recking*, 2009; *Prancevic et al*., 2014], and overpredict the sediment flux by a factor of 10 [*Lenzi et al*., 1999; *Rickenmann*, 2001; *Mueller et al*., 2005; *Yager et al*., 2007; *Nitsche et al*., 2011; *Yager et al*., 2012; *Schneider et al*., 2015]. Thus, sediment is apparently more stable, and fluxes of water and sediment are far lower than expected from comparison with low gradient rivers.

One of the leading hypotheses for higher friction coefficients and lower sediment transport rates in steep streams is that drag from channel forms, bed forms, and immobile obstacles, such as immobile boulders and woody debris, slows the flow by extracting momentum that otherwise would act on the mobile sediment fraction [*Buffington and Montgomery*, 1999; *Millar*, 1999; *Wilcox et al*., 2006; *Yager et al*., 2007; *Nitsche et al*., 2011; *Ferguson*, 2012; *Schneider et al*., 2015]. We refer to drag on these channel forms and large immobile roughness elements as *morphologic form drag* to distinguish it from *grain drag* acting on the mobile or intermittently mobile bed sediment that is transported by fluvial processes. An alternate hypothesis, however, is that the hydraulics of mountain streams differ from lowland rivers even for planar beds that lack complex bed topography because, in mountain streams, the flow depth, h, is typically of the same scale as the bed roughness, k_s, which is proportional to the diameter, D, of cobbles and boulders that line the stream bed [*Kamphuis*, 1974]. Thus, mountain streams dominated by grain drag alone have high relative roughness (k_s/h), which creates complex 3-D flow patterns that may alter the forces of lift and drag on bed sediment, which in turn could affect water velocities and sediment fluxes [*Mizuyama*, 1977; *Bathurst et al*., 1981; *Novak and Nalluri*, 1984; *Cao*, 1985; *Rice et al*., 1998; *Recking et al*., 2008a].

Flume experiments offer a means to isolate the roles of morphologic form drag and grain drag, which are otherwise difficult to separate in mountain streams. For example, identical experiments have been conducted both with and without step-pool bed forms [*Zimmermann*, 2010], and surprisingly these showed similar friction coefficients, suggesting that grain drag may be much larger in steep mountain streams than commonly assumed. Similarly, steep flume experiments with planar beds of gravel yielded friction coefficients similar to the high values observed in steep mountain streams resistance [*Mizuyama*, 1977; *Bathurst et al*., 1981; *Cao*, 1985; *Bathurst*, 2002; *Recking et al*., 2008b; *Prancevic and Lamb*, 2015a; *Lamb et al*., 2017], pointing to the importance of grain drag in determining flow resistance. Laboratory studies of sediment transport for steep, planar beds of uniform sediment also have observed high Shields numbers ($\tau_* = \frac{\tau_b}{(\rho_s - \rho_w)gD}$, where ρ_s is the density of sediment and g is acceleration due to gravity) at initial sediment motion similar to field observations, despite the lack of step pools, immobile boulders or other sources of morphologic form drag [*Mizuyama*, 1977; *Prancevic et al*., 2014; *Prancevic and Lamb*, 2015a]. Together, these studies suggest that the lift and drag forces on bed sediment in steep rivers with high relative roughness may differ from those in lower gradient rivers, even for planar, rough beds that lack morphologic form drag. Moreover, it seems possible that changes in lift and drag forces on the mobile bed sediment may partially account for the lower than expected sediment transport in steep rivers. However, to date, we lack direct measurements of lift and drag on bed particles for conditions common to mountain streams.

The goal of this paper is to evaluate existing hypotheses for reduced sediment transport and heightened flow resistance in steep rivers by direct measurement of lift and drag forces on cobbles in steep flume experiments. Although lift and drag forces have been measured previously, these studies mostly focused on low gradient streams with large water depths relative to the particle size. In section 2, we review this previous work. In section 3, we introduce the experiments and methods used to isolate the lift and drag coefficients from direct force measurements. We discuss the experimental findings on lift and drag coefficients and force fluctuations for different particle sizes, particle shapes, channel-bed slopes, and particle submergence in section 4. Finally, we discuss the implications of our results for predicting flow resistance and sediment transport.

2. Theoretical Considerations

The drag and lift coefficients, C_D and C_L, are used to relate the average downstream drag force, $\overline{F_D}$, and bed-normal lift force, $\overline{F_L}$, to the local downstream directed flow velocity averaged across a grain:

$$\overline{F_D} = \frac{1}{2}\rho_w C_D \langle \bar{u} \rangle^2 A_{sub} \tag{1a}$$

$$\overline{F_L} = \frac{1}{2}\rho_w C_L \langle \bar{u} \rangle^2 A_{sub} \tag{1b}$$

in which $\bar{u}$ is the local downstream flow velocity averaged in time, and the brackets denote a spatial average over the submerged, upstream-facing cross-section area of the particle transverse to flow, A_{sub}. The drag force at large particle Reynolds numbers is due to the pressure difference between the upstream and downstream regions of the particle owing to the wake in the lee of the particle. The origin of the lift force is not as clear. Some have proposed that the velocity scale of interest for lift should be the difference between the downstream velocity at the top of the grain versus the bottom, following the Bernoulli lift force [*Wiberg and Smith*, 1987]. *Schmeeckle et al*. [2007] argued, however, that lift, like drag, is controlled by the wake in the lee of the particle, and any horizontal asymmetry in the wake would induce a component of lift. In this case, $\langle \bar{u} \rangle$ would be the appropriate velocity scale. In practice, the two velocity scales are likely to be proportional to each other [*Wiberg and Smith*, 1987; *James*, 1990; *Lamb et al*., 2008; *Recking*, 2009], and thus we use equation (1b).

Drag coefficients for spheres far from a boundary (free stream) are known to be a function of the particle Reynolds number but are approximately constant, $C_D \sim 0.4$–0.5, for $\mathrm{Re}_p = \langle \bar{u} \rangle D/\nu > 10^3$ (ν is the kinematic viscosity) when wakes are fully turbulent [*Schlichting*, 1979; *Lee and Balachandar*, 2012]. Direct measurements of drag and lift coefficients near a wall have been made only in a few studies, and most of these have analyzed forces on a submerged sphere or hemisphere sitting on a smooth, low-sloping bed in deep flow [*Einstein and El-Samni*, 1949; *Chepil*, 1958; *Roberson and Chen*, 1970; *Cheng and Clyde*, 1972; *Bagnold*, 1974; *Lee and Balachandar*, 2012]. *James* [1990] summarized much of this work and concluded that $C_L \sim 0.5 C_D$ for large particle Reynolds numbers. *Schmeeckle et al*. [2007] made direct measurements of lift and drag over a gravel bed, but also in low gradient streams with deep flow. They found for spherical particles that $C_D \sim 0.76$, C_L was highly variable, and that peak deviations in drag and lift forces due to turbulence were large when particles protruded above the bed [see also *Dwivedi et al*., 2010, 2011; *Lee and Balachandar*, 2017].

Only *Flammer et al*. [1970] directly measured forces on partially submerged particles ($h/D_t < 1$, in which D_t is the diameter of the test particle), and they found that the drag increases significantly as flow depth shallows relative to the particle size and due to surface wave effects as Froude numbers, Fr, approach ~0.6. However, like earlier studies, *Flammer et al*. [1970] used a hemisphere over a smooth bed. They also did not measure lift or the local flow velocity making it difficult to apply their results to steep mountain rivers. For example, *Flammer et al*. [1970] used the depth-averaged velocity, rather than the local velocity ($\langle \bar{u} \rangle$), in equation (1a) such that their reported drag coefficients necessarily increase for shallow flows because of the slower depth average velocity (i.e., greater flow resistance) common to shallow flows. Thus, their reported trends in drag coefficients with flow depth reflect, in part, changes in depth-averaged velocities rather changes in drag forces. Nonetheless, others have inferred that C_D must increase with increasing particle emergence ($h/D_t < 1$) from observations of initial motion of isolated particles or blocks by assuming thresholds for sliding or rolling [*Lawrence*, 2000; *Carling et al*., 2002]. Higher drag coefficients for Fr ~ 0.6 due to surface wave effects also have been measured for flow around vertical cylinders and bridge piers [*Hay*, 1947; *Chaplin and Teigen*, 2003].

Because direct measurements of lift and drag forces are rare, commonly the boundary shear stress, τ_b, is used as a proxy for the drag force acting on a particle per unit area, and the lift force is assumed to be linearly proportional as well [*Chepil*, 1958; *Wiberg and Smith*, 1987; *James*, 1990; *Lamb et al*., 2008; *Recking*, 2009]. Indeed, the boundary shear stress is the basis for the Shields criterion used for initial sediment motion [*Shields*, 1936] and most sediment flux relations [*Meyer-Peter and Müller*, 1948]. Rearranging equation (1), and using the definition $\tau_b = \rho_w u_*^2$, results in

$$\frac{\overline{F_D}}{A_{sub}} = \frac{1}{2} C_D \frac{\langle \bar{u} \rangle^2}{{u_*}^2} \tau_b \tag{2a}$$

$$\frac{\overline{F_L}}{A_{sub}} = \frac{1}{2} C_L \frac{\langle \bar{u} \rangle^2}{{u_*}^2} \tau_b \tag{2b}$$

Equation (2) reveals that the boundary shear stress is only a good proxy for the average drag and lift forces on the particle per unit area if the vertical structure of the normalized near-bed velocity (i.e., $\langle \bar{u} \rangle / u_*$) and

the drag and lift coefficients are constants. For example, if the velocity profile is properly represented by the law of the wall, and for uniform sediment where the bed roughness scale, k_s, is a multiple of the particle D, then $\langle \bar{u} \rangle / u_*$ is a constant. However, the vertical velocity profile can deviate strongly from the log law, especially near the bed in the roughness layer where the flow is strongly affected by bed roughness [*Christensen*, 1972; *Nowell and Church*, 1979; *Wiberg and Smith*, 1991; *Nikora et al*., 2001]. Using different scaling arguments, several workers have proposed that $\langle \bar{u} \rangle / u_*$ in the roughness layer may decrease for shallow, rough flows, thereby producing lower than expected forces on grains (equation (1)) and heighted critical Shields numbers for steep mountain streams [*Lamb et al*., 2008; *Recking*, 2009; *Ferguson*, 2012]. However, more recently, *Lamb et al*. [2017] showed in flume experiments with a planar bed of cobbles that $\langle \bar{u} \rangle / u_*$ deviates from the log law in the roughness layer, but nevertheless it varies little with channel slope, Froude number, and relative roughness across a wide range of these parameters common to mountain streams. If indeed $\langle \bar{u} \rangle / u_*$ varies little with channel slope and relative roughness, then, following equation (2), changes to the mean forces on particles in steep streams, with respect to τ_b, must be due to changes in the drag and lift coefficients.

Fluctuations in forces due to turbulence can also affect sediment transport. For example, the near-bed turbulence, σ_u (i.e., the standard deviation of the downstream oriented velocity near the bed), does not scale with the bed shear velocity as commonly assumed [*Nezu and Nakagawa*, 1993], but instead scales linearly with the depth-averaged flow velocity:

$$\sigma_u = \alpha_1 U_{surf} \tag{3}$$

where $\alpha_1 \approx 0.2$ [*Wang et al*., 1993; *Dittrich and Koll*, 1997; *Carollo et al*., 2005; *Lamb et al*., 2008, 2017]. Thus, the near-bed intensity of turbulence, σ_u / u_*, scales as $C_f^{-1/2}$ (i.e., $\sigma_u / u_* \propto U_{surf} / u_* \equiv C_f^{-1/2}$) and is therefore expected to be smaller for shallow, rough flows. *Lamb et al*. [2008, 2017] argued that reduced near-bed turbulence can partially explain heightened critical Shields numbers in mountain streams. However, the fluctuating components of lift and drag forces have yet to be measured directly in shallow, rough flows.

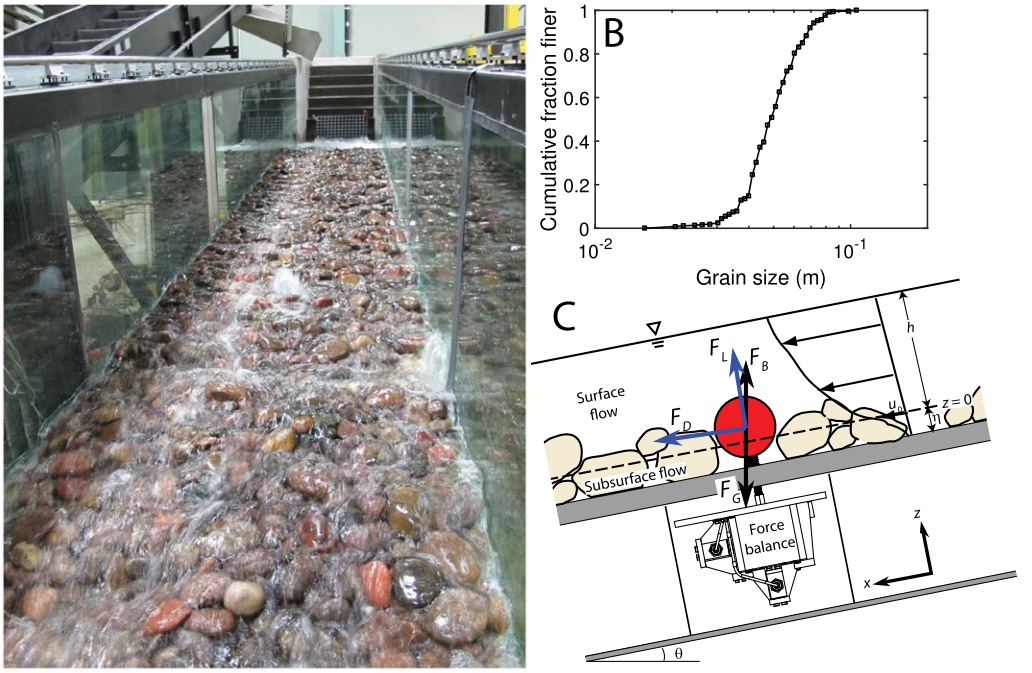

Figure 1. (a) View looking upstream in the flume bed with shallow flow at $S = 0.15$ (similar to experiment set 15 in Table 2). (b) Grain size distribution for the intermediate diameter of cobbles used in the experiments. (c) Schematic cross section of experimental flume showing the force balance below the false floor, test particle (red) and neighboring particles which define the average bed elevation set at $z = 0$, and set the depth of the surface flow (h) and subsurface flow (η). Four forces act on the particle—lift (F_L), drag (F_D), gravity (F_G), and buoyancy (F_B). The test particle was mounted on the rod, and the distance between the flume floor and the bottom of the particle is given as the rod height in Table 1.

Table 1. Properties of Test Particles

Particle Number	Downstream Diameter (m)	Cross-Stream Diameter (m)	Vertical Diameter (m)	Dry Weight (N)	Density (kg/m^3)	Rod Height (m)	Material
3	0.076	0.076	0.076	−3.20	1399	0.005	Acrylic
5	0.125	0.125	0.125	−9.24	909	0.010	Polypropylene
6	0.218	0.218	0.218	−31.00	592	0.014	Bowling ball
7	0.076	0.076	0.076	−2.32	956	0.005	Polypropylene
8	0.218	0.218	0.218	−50.17	948	0.015	Bowling ball
9	0.076	0.076	0.076	−17.89	7764	0.002	Chrome-steel
10	0.161	0.161	0.161	−3.28	152	0.000	Urethane-foam
11	0.152	0.152	0.152	−2.05	128	0.004	Polystyrene-foam
12	0.177	0.177	0.177	−3.08	109	0.009	Polystyrene-foam
13	0.203	0.203	0.203	−3.81	88	0.014	Polystyrene-foam
41	0.125	0.075	0.074	−9.63	2674	0.014	Cobble
42	0.075	0.125	0.074	−9.63	2674	0.015	Cobble

3. Methods

Flume experiments were conducted in a 15 m long, 1 m wide tilting flume at the California Institute of Technology across a range of channel slopes ($0.004 < S < 0.3$) and water discharges ($0.007 < Q < 0.69$ m^3/s) (Figure 1a and supporting information Table S1). We performed 217 different experiments. For each discharge and channel slope combination, we measured the forces on 12 different test particles (Table 1) using a force balance. All flows were fully turbulent ($\mathrm{Re} > 10^3$) and Froude numbers ranged from subcritical to supercritical ($0.29 < \mathrm{Fr} < 7.8$) (Table 2).

All experiments used the same sediment bed consisting of natural river cobbles ($D_{50\text{-bed}} = 49$ mm and $D_{84\text{-bed}} = 64$ mm, in which the subscript denotes the percentile of grains finer; Figure 1b) hand screeded to produce a planar bed with a thickness of about one grain diameter and smooth glass walls (Figure 1a). These grains set the characteristic bed roughness height, for which we use $k_s = 2.5D_{84\text{-bed}}$ [e.g., *Kamphuis*, 1974], and all flows were hydraulically rough ($\mathrm{Re}_{k_s} = u_* k_s / \nu > 10^3$). The cobbles were fixed to the floor using a light coating of epoxy, which did not significantly alter grain roughness or pore geometries. The cobbles were fixed to prevent sediment transport that would otherwise damage the force balance, and to maintain a planar bed that lacked morphologic form drag. We explored conditions that fall both below and well in excess of the expected threshold of sediment motion.

For each experiment, a test particle was fixed to the force balance located near the center of the flume in both width and length. The force balance sat below a false floor in the flume and was totally submerged

Table 2. Hydraulic Properties of the Experiments

Experiment Set	Bed Slope, S	Discharge, Q (m^3/s)	Subsurface Discharge, Q_{sub} (m^3/s)	Depth-Averaged Velocity, U_{surf} (m/s)	Flow Depth, h (m)	Froude Number, Fr	Flow Reynolds Number, Re	Experiment Number From *Lamb et al.* [2017]
8	0.300	0.500	2.10×10^{-2}	3.69	0.13	3.26	4.80×10^5	55
9	0.300	0.024	1.00×10^{-2}	0.34	0.03	0.64	9.50×10^3	50
11	0.300	0.154	1.50×10^{-2}	1.91	0.07	2.25	1.40×10^5	54
12	0.300	0.302	1.33×10^{-2}	3.42	0.10	3.37	3.59×10^5	-
13	0.150	0.492	1.50×10^{-2}	3.08	0.15	2.50	1.40×10^5	46
14	0.150	0.303	7.70×10^{-3}	2.87	0.11	7.80	3.59×10^5	47
15	0.150	0.011	6.20×10^{-3}	0.15	0.03	0.29	1.40×10^5	48
16	0.020	0.499	4.50×10^{-3}	1.84	0.27	1.14	3.59×10^5	17
17	0.020	0.301	3.60×10^{-3}	1.50	0.20	1.08	1.40×10^5	1
18	0.020	0.159	2.80×10^{-3}	1.09	0.14	0.92	3.59×10^5	19
19	0.020	0.031	1.80×10^{-3}	0.39	0.07	0.47	1.40×10^5	20
20	0.150	0.166	1.10×10^{-2}	1.76	0.09	1.89	3.59×10^5	45
21	0.080	0.289	8.60×10^{-3}	2.09	0.13	1.82	1.40×10^5	37
22	0.080	0.392	9.60×10^{-3}	2.39	0.16	1.90	3.59×10^5	39
23	0.080	0.153	7.00×10^{-3}	1.51	0.10	1.55	1.40×10^5	40
24	0.080	0.030	4.90×10^{-3}	0.48	0.05	0.68	3.59×10^5	41
25	0.004	0.031	4.90×10^{-4}	0.30	0.10	0.30	1.40×10^5	7
26	0.004	0.154	9.10×10^{-4}	0.69	0.22	0.47	3.59×10^5	10
27	0.004	0.323	1.30×10^{-3}	0.96	0.34	0.53	1.40×10^5	11
28	0.004	0.514	1.60×10^{-3}	1.21	0.42	0.60	3.59×10^5	13

within a compartment with no flow around the balance (Figure 1c). The particles were fastened to the force balance using a metal rod, which was embedded within the particle. We investigated a natural cobble that was selected from the mixture used to make the bed, a foam particle carved to be roughly spheroidal, and a variety of spheres of different densities (Table 1). The spheres were made of different materials with a range of densities to verify that the force balance yielded accurate submerged weights; these included chrome-steel, acrylic, plastic-foam, and bowling balls (wood cores and plastic exteriors) (Table 1). The intermediate diameter of the test particles, D_t, ranged from 75 to 218 mm. Particle weight was measured using a scale accurate to 1 g ($\sim$0.01 N), and particle volume was measured for larger spheres by measuring the diameter at two locations using a micrometer. Smaller and nonspherical particles were submerged in a container and the change in water surface elevation was measured to sub-mm resolution with a Keyence laser. The volumes are accurate to $<$5% for all particles, and $\sim$1% on average. An effort was made to locate the test particles as close to the flume floor as possible, while maintaining separation between the test particles and the epoxied particles on the bed. This distance ranged from 5 to 15 mm (*rod height* in Table 1). The rod width was 11.65 mm, and the exposed area of the rod was a negligible fraction of the surface area of the particle even at low submergence. Thus, the force-balance measurements recorded hydraulic forces, and particle weight and buoyancy, with no contact forces between neighboring particles. The larger test particles necessarily sat higher into the flow, resulting in larger values of $D_t/D_{50\text{-bed}}$.

3.1. Force Balance Calibration and Decomposition

The force balance was custom made and used two Flintec PC6 load cells with 0.03 N reported accuracy to measure forces in the downstream, F_x (where x is the downstream coordinate) and flume-bed normal, F_z (where z is the flume-normal coordinate that is positive up) directions (Figure 1c). These bridge-type load cells measure the change in electrical resistance of a component as it is deformed under load. The load cells have $<$0.01% change in reading over a 10°C temperature range. All signal wiring had grounded shielding to prevent magnetic interference. To calibrate the force balance, we built a low-resistance pulley and cable system to isolate the components of lift and drag. Known weights were used to build a calibration curve between static force and digitized output signal. Through repeated cycles of loading and unloading of known weights, we found the force balance had a resolution of 0.1 N under these controlled conditions.

The above calibrations were made while the force balance was dry and horizontal. To apply the calibrations while the force balance was submerged and tilted in the flume, we needed to account for the weight of the force balance components and how they shift to produce a measured load. To examine this, we attached a particle of known weight to the force balance and tilted the flume bed to a known slope. The flume was filled brimful with water and sealed off to produce a pond with no flow that fully submerged the test particle; these measurements were necessarily limited to lower flume slopes in order to impound the water ($S < 5\%$). For each test particle, we compared the output drag and lift from the force balance with known loads that consisted only of the submerged particle weights, the submerged weight of the balance, $W_{b,sub}$, and a constant tare or offset, so that the measured forces equaled:

$$F_x = \left((\rho_s - \rho_w)gV + W_{b,sub}\right)\sin\theta + tare_{x,sub} \tag{4a}$$

$$F_z = -\left((\rho_s - \rho_w)gV + W_{b,sub}\right)\cos\theta + tare_{z,sub} \tag{4b}$$

in which V is the volume of the test particle, and $tare_{x,sub}$ and $tare_{z,sub}$ are the constant offsets in the x and z directions. The flume slope angle, θ, is taken to be positive when tilting downstream, and $S = \tan\theta$. The results from measurements at several bed angles allowed us to find the effective submerged weight of the force balance, $W_{b,sub}$, from the slope of the linear fit (e.g., Figure 2a), and the tare values as the y-intercepts. This procedure was repeated for each test particle and for a range of bed slopes. The standard deviation of tare values from this analysis indicates that the force balance has an uncertainty in the mean load measurements of $\sim$0.3 N in lift and drag. These values are larger than the uncertainties from the dry force balance calibration because of drifts in the force balance calibration due to time, temperature fluctuations, wetting and drying, and loading and unloading, during the experiments.

The force balance also has a resonant frequency. To identify this frequency, we pinged the force balance while fully submerged with a single impulse from a stiff hammer and analyzed its response using a sampling frequency of 4000 Hz. Power spectral density plots show a strong resonant response at $\sim$45 and 60 Hz for F_x and F_z, respectively (Figure 2b). The signal also shows significant instrument noise at frequencies

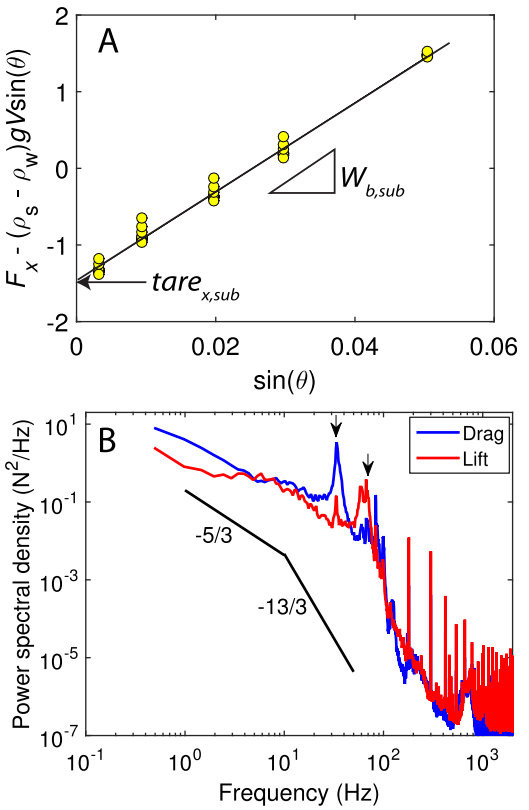

Figure 2. (a) Submerged force-balance measurements for multiple test particles at multiple flume slopes plotted following equation (4) to isolate any constant offset, or tare, between the measurements and the absolute force. (b) Typical power spectral density plot of force balance data showing resonance at 35 and 65 Hz for drag and lift, respectively (arrows). Example shown is from experiment 281 (supporting information Table S1) at $S = 0.15$ and $h/D_t = 0.8$.

greater than 100 Hz. To remove the power at the resonant frequencies and noise at higher frequencies we applied a fifth-order low-pass Butterworth filter to all force-balance measurements with a cutoff frequency of 30 Hz. Most of the power in force fluctuations occurs in the largest scales of turbulence (e.g., <10 Hz in the experiments; Figure 2b). For frequencies greater than 1 Hz, there is a steep fall off in turbulent energy with frequency to the −5/3 power, as expected for the inertial subrange in the turbulent energy cascade [*Tennekes and Lumley*, 1972]. Moreover, *Gimbert et al.* [2014] showed theoretically that particle force fluctuations are expected to fall off at −13/3 power at high frequencies that correspond to eddies smaller than the particle, which is evident in our force data (Figure 2b). This steeper falloff occurs because the positive and negative excursions from smaller eddies offset each other when spatially averaged over the particle. Thus, the low-pass filter applied to our data should have little effect on the standard deviation of forces analyzed herein. Using the theory of *Gimbert et al.* [2014], we estimate less than 10% reduction in the standard deviation of forces due to the filtering scheme.

Ultimately, we want to measure the force exerted on the particle from flowing water in the downstream x direction due to drag, F_D, and in the bed-normal z direction due to lift, F_L (Figure 1c). In addition, in some cases, the test particles were only partially submerged, which affects particle buoyancy. During an experiment with flowing water, the force balance measured the same components as in the still water tests (equation (4)), and in addition the drag and lift forces, such that

$$F_x = F_D + \left(\rho_s g V - \rho_w g V_{sub} + W_{b,sub}\right)\sin\theta + tare_{x,sub} \tag{5a}$$

$$F_z = F_L - \left(\rho_s g V - \rho_w g V_{sub} + W_{b,sub}\right)\cos\theta + tare_{z,sub} \tag{5b}$$

in which V_{sub} is the submerged volume of the test particle. If V_{sub} is known (discussed in section 3.2), and since $W_{b,sub}$, $tare_{x,sub}$, and $tare_{z,sub}$ are known from the calibration procedure that yielded equation (4), then equation (5) can be rearranged to solve for the drag and lift forces, F_D and F_L. Reported error bars represent ±0.3 N.

3.2. Buoyancy of Partially Submerged Particles

For a fully submerged particle, the buoyancy force, F_B, follows Archimedes principle: $F_B = \rho_w g V$ under the assumption of a hydrostatic pressure distribution and acts positive upward in the vertical direction. *Christensen* [1995] questioned whether buoyancy should be taken as normal to the water surface, rather than vertical, for sloping shear flows; however, *Chiew and Parker* [1995] showed that the integration of normal and shear forces acting on a particle renders buoyancy vertical even for moving flows with a sloping water surface, at least for gradually varied flow in which the pressure distribution is approximately hydrostatic.

In some of our experiments, the particle tops were partially emerged from the flow (Figure 3), so that the buoyancy force becomes $F_B = \rho_w g V_{sub}$, and this requires a calculation of the submerged volume of the particle. We calculated the submerged particle volume by approximating the particle shapes as ellipsoids and

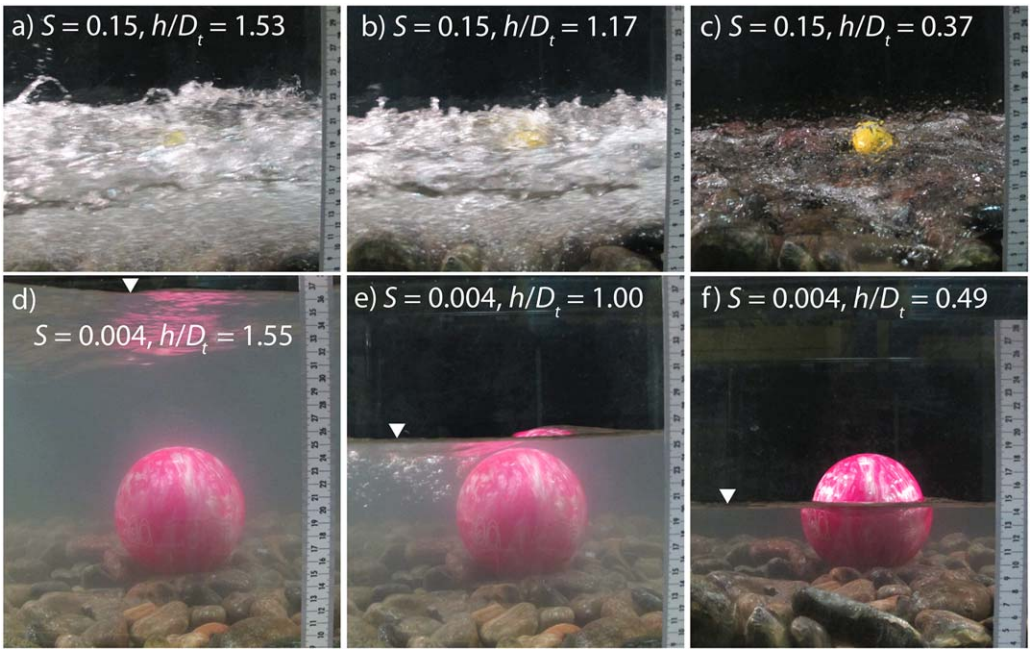

Figure 3. Pictures of test particles on the force balance for a range of relative flow depths and at (a–c) a steep bed slope, $S = 0.15$, with $Fr > 1$, and (d–f) a low bed slope, $S = 0.004$, with $Fr < 1$. In Figures 3a–3c, the particle is a natural cobble (particle number 42 in Table 1), and in Figures 3d–3f, the test particle is a bowling ball (particle number 6 in Table 1). Hydraulic conditions are given in Table 2 and the experiment set numbers are 14, 20, 15, 27, 26, and 25 for Figures 3a–3f, respectively. Flow is from right to left. Scale bar on right is in centimeters.

integrating the volume of a partially submerged ellipsoid [see for example, *Lamb et al.*, 2008]. When the average water surface elevation was near the top of the test particle, the flow over the test particle was complex and in cases included shooting flow ("rooster tails"), flow that ramped up the upstream side of the particle and spilled down the downstream side of the particle, and standing waves (Figure 4). Due to the complex water surface topography, the particle was often visually wet even though the particle top was higher than the elevation of the average water surface in the test section. Many of these flow configurations likely violated the hydrostatic pressure assumption over the top of the particle. Thus, to calculate submerged volume of the particle and the buoyancy force acting on the test particle, we used the average water surface elevation in the test section of the flume rather than the local water surface elevation, and again took buoyancy to act in the vertical direction. Water surface elevations during each experiment were measured using a Massa ultrasonic probe at 50 mm spacing and 1 mm accuracy. Because the force balance measures the total applied force of buoyancy plus lift and drag, any effects from the dynamic water surface, including shooting flow, waves, and nonhydrostatic effects in the buoyancy force, are therefore assumed to be part of the lift and drag forces by this definition.

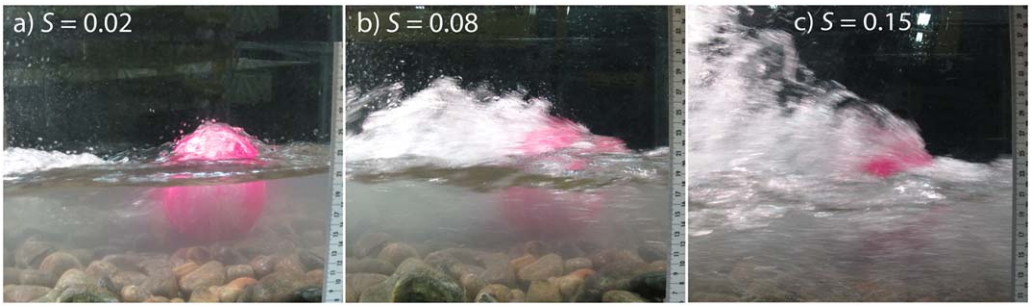

Figure 4. Pictures of test particle 6 showing differences in the wake as function of bed slope, all with $h/D_t \sim 0.7$: (a) experiment set 18 with $S = 0.02$ and $Fr = 0.92$, (b) experiment set 22 with $S = 0.08$ and $Fr = 1.9$, and (c) experiment set 13 with $S = 0.15$ and $Fr = 2.5$. Hydraulic conditions are given in Table 2. Flow is from right to left. Scale bar on right is in centimeters.

Finally, for some of the steep experiments investigated, the flows were visibly aerated. Aeration can change the density of the fluid, which can affect our calculation of buoyancy. From continuity, $\rho_w = \rho_{w0}(1-c_a)$, in which ρ_{w0} is the density of water for air-free conditions, and c_a is the volumetric concentration of air. Water temperature in the experiments ranged from 23 to 28°C, and thus $\rho_{w0} = 1000$ kg/m^3 within 0.4% uncertainty. We did not measure the aeration directly, but we take it into account using the relation of *Chanson* [1994], $c_a = 0.9\sin\theta$, which is based on fully turbulent experiments [*Straub and Lamb*, 1956; *Aivazyan*, 1987]. For our experiments, the aeration correction to water density has negligible effect on the results.

3.3. Velocity Measurements

Measurements of flow velocity at the location of the test particle are required to calculate the lift and drag coefficients following equation (2). These measurements were made in a series of companion experiments with the test particle removed [*Lamb et al*., 2017], but otherwise were identical to the bed and flow conditions of the main experiments. The test particle was removed to make measurements of the representative flow velocity in the absence of disturbance caused by the particle. A detailed analysis of the vertical velocity profiles and friction factors from the companion experiments is presented in *Lamb et al*. [2017], and relevant methods and findings are briefly summarized here.

Total discharge into the flume, Q, was measured using a Rosemount in-line magnetic flow meter. The bed and water surface elevations were measured using a motorized cart with millimeter-resolution positioning. A laser distance meter with sub-mm vertical accuracy was used to measure the topography of the flume bed at a spatial resolution of 1 mm, and the average bed elevation along the centerline of the test section is taken as $z = 0$ (Figure 1c). The average alluvial bed elevation sat above the impermeable floor of the flume, creating a thin but important zone of subsurface flow of thickness $\eta = 28$ mm (Figure 1c). The difference between the average water surface and bed elevations was defined as the flow depth, h, for each experiment. For each experimental configuration, we adjusted the inlet and outlet conditions in the flume to ensure uniform cross-sectionally averaged flow in the center 10 m of the flume, referred to as the test section. The smooth walls were found to contribute to a negligible (<2%) fraction of the total drag owing to the rough bed and large width-to-depth ratios. Thus, we verified steady and uniform flow averaged over the test section and approximate the average bed shear stress as $\tau_b = \rho g h \sin\theta$.

Flow velocity was measured using a single vertical profile located where the test particles were later mounted to the force balance in the center of the test section. We measured flow velocity at 200 Hz for 120 s at about ten points in the z dimension (subvertical) using a side looking Nortek acoustic Doppler profiler (ADV). A void between neighboring cobbles ~5 cm to the side of the measurement location allowed the probe to be lowered into the roughness layer. The velocity time series were deconvolved into time averages, $\bar{u}$, and fluctuating components.

It was not possible to make measurements of velocity in the steepest cases (bed slope, $S = 30\%$) with an ADV due to fast and aerated flows. Instead, for these cases, we used the flow velocity model developed and tested in *Lamb et al*. [2017] (Figure 5a). Following *Christensen* [1972], they derived a flow velocity model using a mixing length argument for surface flow ($z > 0$) both within and above the roughness layer, which resulted in

$$\frac{\overline{u}(z) - u_0}{u_*} = \frac{1}{\kappa} \ln\left(1 + \frac{30z}{k_s} \exp\left(-\kappa \frac{u_0}{u_*}\right)\right) \tag{6}$$

in which u_0 is the flow velocity at $z = 0$ due to subsurface flow (Figure 1c), and $\kappa = 0.41$ is von Kármán's constant. Equation (6) approaches the typical log law, $\frac{\overline{u}(z)}{u_*} = \frac{1}{\kappa} \ln\left(\frac{30z}{k_s}\right)$, high above the bed ($z \gg k_s$) for cases without subsurface flow, and produces a more uniform velocity profile near the bed due to changes in the hydraulics in the roughness layer [*Nikora et al*. 2001]. For the steepest slopes of concern here, the subsurface flow ($z < 0$) was nonnegligible, and *Lamb et al*. [2017] derived a modified Darcy-Forchheimer-Brinkman equation for the flow velocity at $z = 0$,

$$u_0 = \frac{C_2}{2\phi_{sub}} \sqrt{\left(\frac{1}{C_1 K F^*}\right)^2 + \frac{4S}{C_1 F^*}\left(\frac{h}{P} + 1\right)} - \frac{1}{2}\frac{1}{C_1 K F^*} \tag{7}$$

in which $K = \frac{gk}{\nu}$ is the hydraulic conductivity, $F^* = \frac{F\phi_{sub}}{g\sqrt{k}}$, $-S$ is the head gradient (which in our case is the negative of bed slope), $k = 10^{-7}$ m^2 is the permeability, $F = 5 \times 10^{-3}$ is the Forchheimer coefficient, and

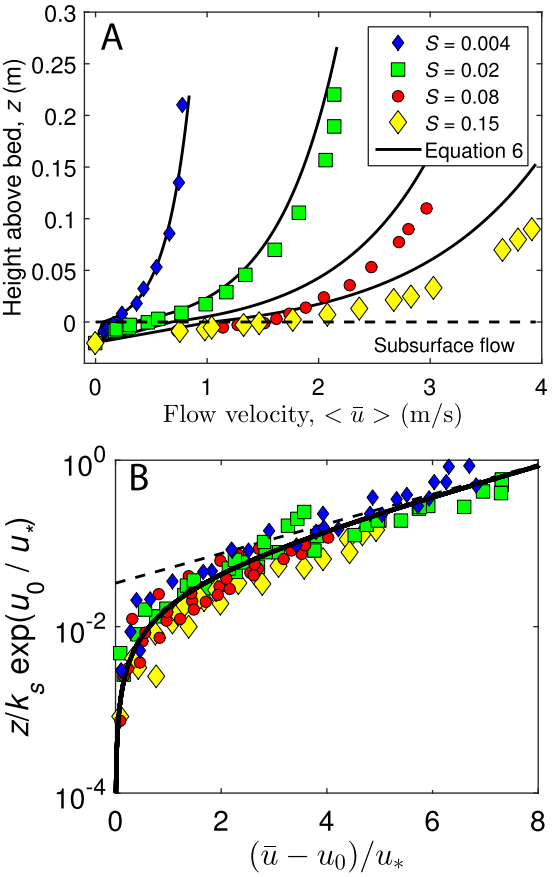

Figure 5. (a) Example velocity profiles from four experiment sets with different bed slopes, *S*, from ADV measurements as reported in *Lamb et al.* [2017], model predictions given by equation (6) for surface flow and an assumed linear profile for subsurface flow ($z < 0$). (b) Collapse of all 15 velocity profiles (including those in Figure 5a) measured by *Lamb et al.* [2017] for the surface flow following equation (6). The dashed line in Figure 5b represents the log law, and the data systematically deviate from the log law near the bed, in the grain roughness layer.

$\phi_{sub} = 0.5$ is the porosity in the subsurface. All values are set following *Lamb et al.* [2017]. C_1 and C_2 are factors that describe the shape of the subsurface flow profile and are both set to two, corresponding to a linear velocity profile in the exchange layer with the subsurface [*Nikora et al.*, 2001]. P is the depth within the exchange layer, where subsurface flow is affected by shear from the overlying fluid [*Nepf and Vivoni*, 2000; *Ghisalberti*, 2009]. We set $P = \eta = 28$ mm, which is the total thickness of the subsurface layer in the experiments [*Lamb et al.*, 2017]. Equation (7) accounts for subsurface flow that is driven both from shear of the overriding surface flow and from the gravitational force acting directly on the subsurface flow due to the sloping bed. Equation (7) also accounts for highly energetic subsurface flow by inclusion of the Forchheimer term.

Figure 5a shows representative velocity profiles from ADV measurements for low and steep sloping experiments, and comparison with the model (equations (6) and (7)). All cases show a near linear velocity profile in the subsurface flow that changes to near logarithmic high above the bed, with a transition region in the roughness layer. When normalized by the subsurface velocity, all velocity profiles collapse to a similar form despite widely varying channel-bed gradients ($0.004 < S < 0.15$) and relative roughness ($0.31 < k_s/h < 4.5$) (Figure 5b). The similarity collapse in Figure 5b, as predicted by equation (6), is important because it indicates that the vertical structure of the local time-averaged velocity, $\bar{u}(z)/u_*$, is not a function of channel-bed slope (S) or relative roughness (k_s/h), except for their minor influence on the subsurface velocity (equation (7)). Therefore, following equation (2), and for cases with similar or negligible u_0, any systematic changes to the time-averaged lift and drag forces with increasing channel slope and relative roughness must be due to changes in the drag and lift coefficients.

Following *Lamb et al.* [2017], the depth-averaged surface flow velocity, U_{surf}, was calculated by integrating the ADV velocity profiles, and for cases without velocity profiles from continuity as $U_{surf} = Q_{surf}/(hW)$, where $W = 1$ m is the flume width. The Froude number was calculated as $Fr = U_{surf}/\sqrt{gh}$. The surface discharge was calculated as $Q_{surf} = Q - Q_{sub}$, the subsurface discharge as $Q_{sub} = U_{sub}\eta W$, and the subsurface velocity as $U_{sub} = \phi_{sub}u_0/C_2$ using equation (7).

3.4. Mean and Fluctuating Lift and Drag Forces

Force data were collected for a given particle, bed slope, and discharge for a duration greater than 60 s. We decomposed the measured time series of lift and drag forces, F_D and F_L, into temporal averages (denoted by overbar) and a fluctuating component (denoted by prime), and used the standard deviation to characterize the fluctuating component. That is

$$\bar{F}_D = \frac{1}{T}\int_0^T F_D dt \tag{8a}$$

$$\bar{F}_L = \frac{1}{T}\int_0^T F_L dt \tag{8b}$$

$$F'_D = \sqrt{\frac{1}{T}\int_0^T (F_D - \bar{F}_D)^2 dt} \tag{9a}$$

$$F'_L = \sqrt{\frac{1}{T}\int_0^T (F_L - \bar{F}_L)^2 dt} \tag{9b}$$

in which T is the total duration of the record. Equation (8) was combined with equation (2) to find the average lift and drag coefficients. The spatial average velocity in equation (2), $\langle \bar{u} \rangle$, was calculated by averaging $\bar{u}(z)$ across the submerged portion of the upstream-facing cross-sectional area of the particle by approximating the particle as an ellipsoid and by assuming negligible lateral gradients in velocity ($d\bar{u}/dy \approx 0$, where y is the cross-stream coordinate) across particle. The lateral velocity gradients were small near the test particle because the test particles were far from the flume walls, and the flume walls were hydraulically smooth. Thus, the spatial average velocity was calculated as $\langle \bar{u} \rangle = \frac{1}{A_{sub}} \int_{z_b}^{z_t} \bar{u}(z) w_p(z) dz$, in which z_b and z_t are the elevations at the bottom and top of the submerged portion of the particle and $w_p(z)$ is the width of the upstream-facing cross section of the particle (i.e., $A_{sub} = \int_{z_b}^{z_t} w_p(z) dz$). Instrument resolution for force fluctuations is expected to reflect the uncertainty in the dry force balance calibration of 0.1 N, rather than 0.3 N for the wet calibration, because isolating the turbulent fluctuations does not rely on estimates of buoyancy, force balance self-weight, or tares, because these quantities do not have fluctuating components.

We were unable to measure the instantaneous lift and drag coefficients because we did not have temporally synchronized velocity and force balance data [see for example, *Schmeeckle et al.*, 2007]. Instead, we define drag and lift coefficients that are associated with fluctuating forces, C'_D and C'_L, following equation (1):

$$F'_D = \frac{1}{2}\rho_w C'_D \sigma_u^2 A_{sub} \tag{10a}$$

$$F'_L = \frac{1}{2}\rho_w C'_L \sigma_u^2 A_{sub} \tag{10b}$$

Combining equations (10) and (3) and rearranging results in

$$C'_D = \frac{F'_D}{0.5\rho_w \alpha_1^2 U_{surf}^2 A_{sub}} \tag{11a}$$

$$C'_L = \frac{F'_L}{0.5\rho_w \alpha_1^2 U_{surf}^2 A_{sub}} \tag{11b}$$

with $\alpha_1 = 0.2$ representing the ratio of near-bed velocity fluctuations to the depth-averaged velocity (equation (3)), which was confirmed from the ADV measurements in our companion experiments [*Lamb et al.*, 2017].

4. Results

4.1. Time-Averaged Drag and Lift Forces

The time-averaged drag forces range from 0.3 to 80 N, with significant uncertainty for the small measured forces due to instrument error of ~0.3 N (Figure 6a). All the particles together show a linear increase in drag force with increasing $\rho_w \langle \bar{u} \rangle^2 A_{sub}$ as expected (equation (2)), with most points falling between $0.1 < C_D < 1$. However, the data are scattered, and some points fall outside these bounds. The data are far more scattered in lift with measured lift forces that range from −35 to 25 N (Figure 6b). Negative lift corresponds to a force directed into the bed, and these measurements are especially common in the experiments with steep bed

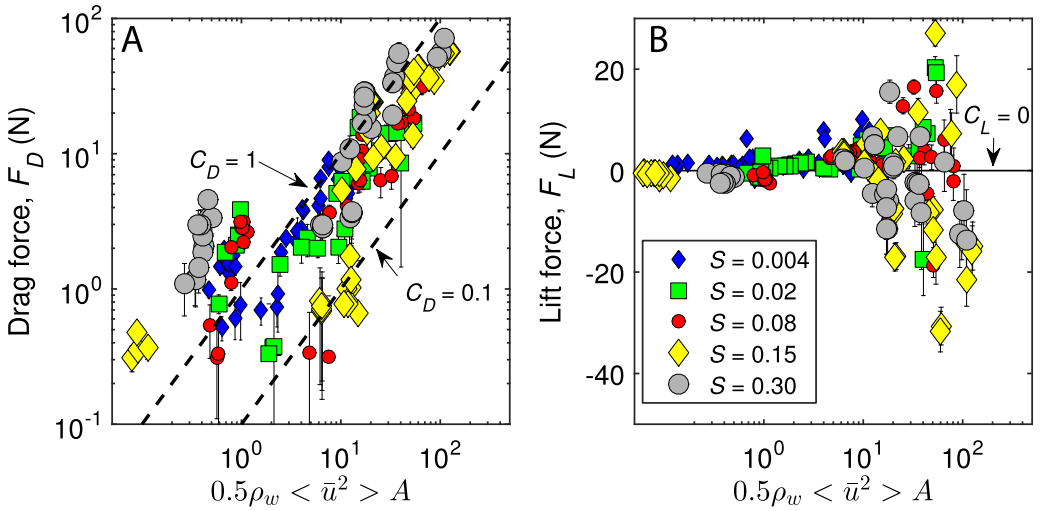

Figure 6. Measured (a) drag and (b) lift forces as a function of the local flow velocity at the particle (see equation (1)) for all particles and five different bed slopes investigated. The error bars represent the standard deviation in instantaneous forces due to turbulence.

slopes when particles were only partially submerged. To explore further the controls on lift and drag, we normalize the forces by $0.5\rho_w\langle\bar{u}\rangle^2 A_{sub}$ to calculate the lift and drag coefficients (equation (2)) and report these as a function of relative particle size, particle Reynolds number, Froude number, and relative submergence. The most important factor controlling lift and drag coefficients from these experiments is the degree of submergence of the test particle for shallowly submerged particles. Before discussing those results, it is first useful to show the results for fully submerged particles.

4.2. Fully Submerged Particles

Limiting the analysis to cases with only deeply submerged particles ($h/D_t > 2$), drag coefficients for spheres increase systematically with $D_t/D_{50\text{-}bed}$ from $C_D \sim 0.1$ for $D_t/D_{50\text{-}bed} = 1.5$ to $C_D \sim 0.7$ for $D_t/D_{50\text{-}bed} > 3$ (Figure 7a). The larger test particles necessarily protruded farther above the bed into the flow (Figure 3); however, the effect of exposure to faster velocities higher in the flow is already accounted for in our calculation of C_D through $\langle\bar{u}\rangle$. Thus, we interpret the reduction in C_D for smaller D_t to be a result of changes in the wake at the lee of the particle, or interactions with the wakes from upstream particles, due to the test particle being immersed between neighboring particles [*Schmeeckle and Nelson*, 2003; *Schmeeckle et al.*, 2007]. The drag coefficients of the nonspherical particles are similar to the spheres. The natural cobble has a slightly smaller C_D as compared with the spheres with its long axis parallel to flow (particle 41) and a slightly larger C_D with its long axis oriented cross stream (particle 42; Figures 3a–3c). The lift coefficients for fully submerged particles vary from $0.06 < C_L < 4$ and show no systematic trends with $D_t/D_{50\text{-}bed}$ or particle shape.

To assess the effect of particle Reynolds number, $\mathrm{Re}_p = \langle\bar{u}\rangle D_t/\nu$, and the possible drop in C_D at high Reynolds numbers due to the drag crisis [*Schlichting*, 1979], we isolate the data to include fully submerged particles ($h/D_t > 2$) that lack significant changes in C_D due to protrusion above the bed ($D_t/D_{50\text{-}bed} > 2$; Figure 7a). Figure 7c shows a slight trend of decreasing C_D with increasing particle Reynolds numbers for the nonspherical particles; however, the spherical particles show no such trend. The lift data again do not show an apparent trend.

4.3. Effect of Froude Number and Particle Submergence

In this section, we analyze all the data with $D_t/D_{50\text{-}bed} > 2$ to eliminate any covarying effects with relative particle size (Figure 7a) as a function of Froude number, Fr, and particle submergence, h/D_t. Figure 3 illustrates the effect of relative submergence for a steep case: $S = 0.15$ with $\mathrm{Fr} > 1$ (Figures 3a–3c), and for a low gradient case: $S = 0.004$ and $\mathrm{Fr} < 1$ (Figures 3d–3f). For the supercritical Froude number experiments ($\mathrm{Fr} > 1$), the water surface was rough (Figure 3a), and for $h/D_t \leq 1$ the flow transitioned from spilling over the test particle, to splitting around the test particle, with chutes and standing waves at the particle scale (Figure 3c). In contrast, for the subcritical Froude number experiments ($\mathrm{Fr} < 1$), the water surface was smooth for both large h/D_t (Figure 3d) and small h/D_t (Figure 3f), but often showed a water-surface wave

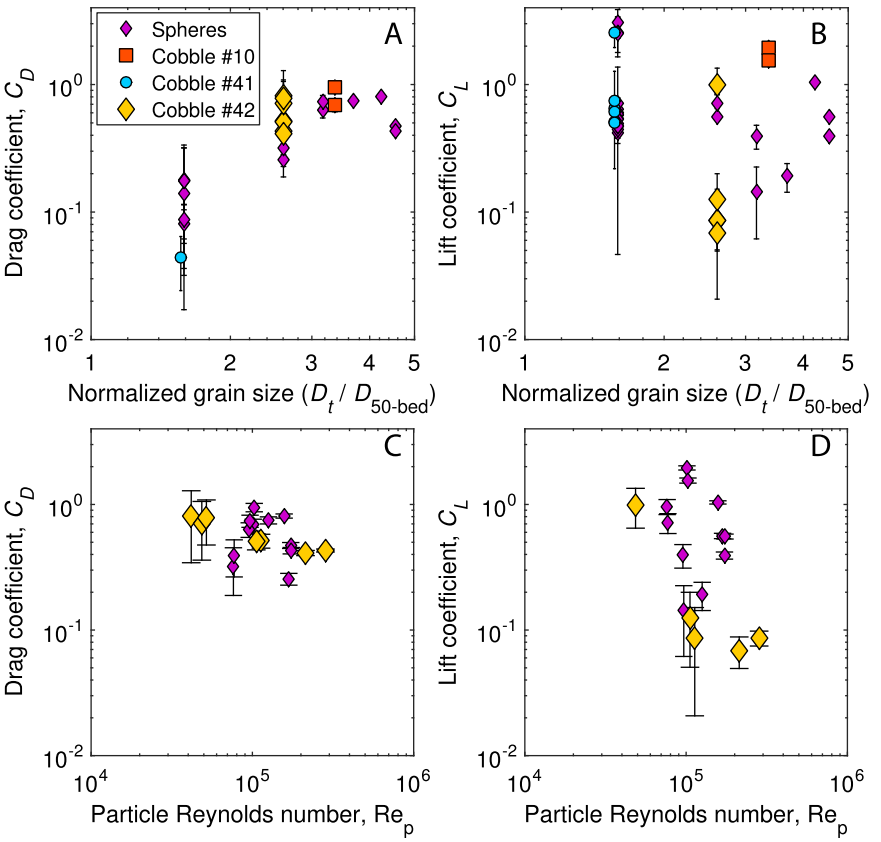

Figure 7. (a, c) Drag and (b, d) lift coefficients for spheres and nonspherical cobbles. (a, b) Only fully submerged particles ($h/D_t > 2$) are shown as a function of the test particle size normalized by the bed sediment size, $D_t/D_{50\text{-bed}}$. (c, d) Fully submerged particles ($h/D_t > 2$) with $D_t/D_{50\text{-bed}} > 2$ as a function of particle Reynolds number. Cobble number 10 (Table 1) is a spheroidal foam particle, not a perfect sphere. Cobble number 41 is a natural cobble representative of the flume bed with its long axis oriented downstream, and cobble number 42 is the same particle with the long axis oriented cross stream. Error bars represent instrument error of 0.3 N.

when $h/D_t \approx 1$. That is, the water surface elevation was raised at the upstream end of the particle, water spilled over the top of the particle in a jet directed toward the bed, and the water surface was depressed in the lee of the particle (Figure 3e). Figure 4 shows the effect of increasing channel slope (and Froude number) on a large particle for cases with nearly identical submergence ($h/D_t \sim 0.7$). At $S = 0.02$, we observed a similar water-surface wave to that at $S = 0.004$ (Figure 3e), but with an increased amplitude on the stoss side of the particle and an increased depression on the lee side of the particle (Figure 4a). As the bed slope increased further, the water no longer spilled down the lee side of the particle, but instead formed a jet that sprayed into the air with increasing vigor (Figures 4b and 4c).

Figure 8 shows that for $Fr < 1$, the drag coefficient increases to values near unity with decreasing Fr. For $Fr > \sim 1$, the drag coefficient appears to be independent of Fr and equal to $C_D \sim 0.4$ for fully submerged particles. Across the full range in Froude numbers, drag coefficients are larger for partially submerged particles ($h/D_t < 1$) as compared with fully submerged particles. The lift coefficient data are scattered and appear to decrease with increasing Fr.

Owing to the apparent change in behavior at $Fr \approx 1$ in Figure 8, we plot the data as a function of relative submergence for $Fr > 1$ (Figures 9a and 9b) and $Fr < 1$ (Figures 9c and 9d) separately. For large Froude numbers, and despite the wide range in bed slopes investigated, C_D is approximately constant for submerged particles with a median value of $C_D = 0.4$ (Figure 9a). However, C_D increases systematically with particle emergence for $h/D_t < 1$, with C_D approaching unity for $h/D_t < 0.5$. The open symbols in Figure 9 show effective force coefficients assuming a buoyancy force for fully submerged particles, whereas the filled symbols are for the calculation of buoyancy accounting for partially submerged particles as described in section 2. Thus, assuming fully submerged particles in the buoyancy calculation results in an even larger apparent C_D. Following equation (2), the drag coefficient is calculated using the flow velocity acting on the submerged

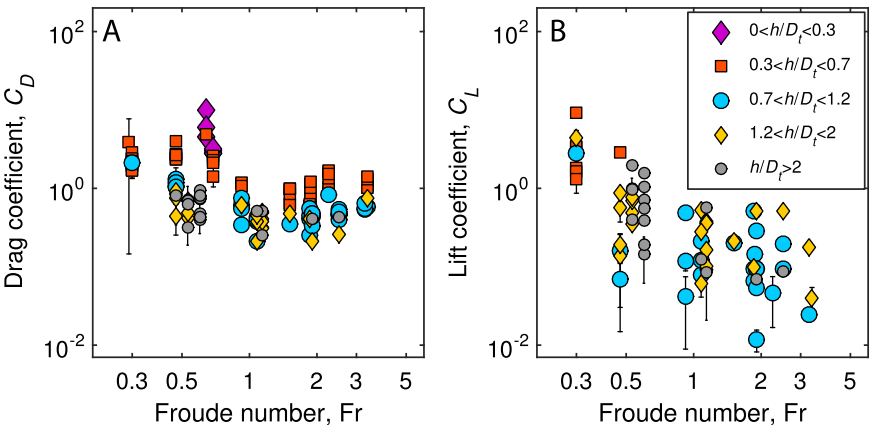

Figure 8. (a) Drag and (b) lift coefficients as a function of Froude number and relative particle submergence, h/D_t for all experiments with $D_t/D_{50\text{-}bed} > 2$. Error bars represent instrument error of 0.3 N.

portion of the particle only, so that the change in C_D with particle emergence cannot be explained simply as a result of a change in the submerged particle area. Instead, we interpret the increase in C_D with particle emergence to reflect changes in pressure around the submerged portion of the particle owing to more tortuous flow deeper within the roughness layer. We find a reasonable fit to C_D for Fr > 1 using

$$C_D = C_{D,sub}\left(\frac{h}{D_t}\right)^{-1.5} \quad \text{for} \quad h/D_t < 1 \tag{12}$$

$$C_D = C_{D,sub} \quad \text{for} \quad h/D_t \geq 1$$

where $C_{D,sub} = 0.4$ is the median drag coefficient for fully submerged particles.

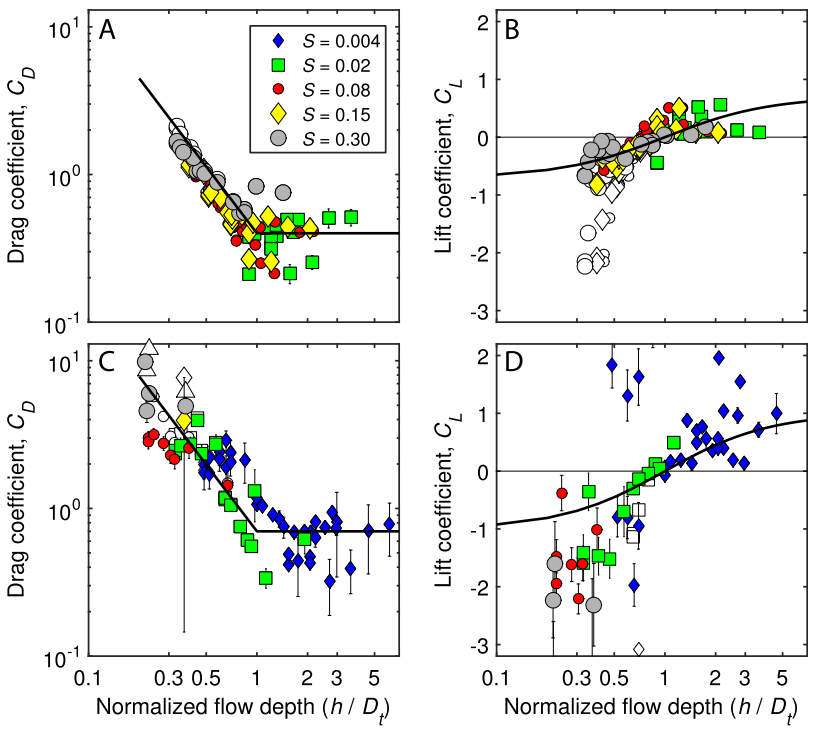

Figure 9. (a, c) Drag and (b, d) lift coefficients as a function of relative particle submergence, h/D_t, shown for supercritical flows (Fr > 1) in Figures 9a and 9b and subcritical flows (Fr < 1) in Figures 9c and 9d. Only experiments with $D_t/D_{50\text{-}bed} > 2$ are shown. Open symbols show results if the correction to buoyancy for partially submerged particles was neglected. Error bars represent instrument error of 0.3 N. The solid lines are equation (12) for drag and equation (13) for lift.

For subcritical flows, the drag coefficients are in general larger than for cases with higher Froude numbers and show considerably more scatter with respect to h/D_t (Figure 9c). For fully submerged particles, C_D is about twice as large for Fr < 1 with C_D ranging from 0.25 to 1. Equation (12) can represent C_D for Fr < 1 with $C_{D,sub} = 0.7$. For the lowest gradient experiments ($S = 0.004$), C_D has a humped relationship with h/D_t in which C_D rapidly increases from ~0.5 to 3 as h/D_t decreases from 2 to 0.8, and then drops as h/D_t decreases below 0.8. The experiments at $S = 0.02$ show a similar relationship with C_D reaching as high as 3.5, and the peak in C_D is shifted to slightly shallower flow with $h/D_t = 0.5$.

In contrast to drag, as the flow shallows relative to the test particle, C_L systematically decreases, becomes negative for partially submerged particles, and approaches $C_L \sim -1$ for $h/D_t \approx 0.5$ (Figure 9b). Given the symmetry in C_L about $h/D_t = 1$, we find a good representation of the data for $h/D_t > 0.5$ across the full range in bed slopes with a hyperbolic tangent function:

$$C_L = C_{L,sub} \tanh\left[0.7 \ln\left(\frac{h}{D_t}\right)\right] \tag{13}$$

in which $C_{L,sub}$ is the value of C_L for well submerged particles (e.g., $h/D_t > 3$). Cases with Fr < 1 show a similar trend but with larger magnitude lift coefficients, and more scattered data with outliers exceeding $C_L = 2$ for $h/D_t > 1$ and $C_L = -2$ for $h/D_t < 1$ (Figure 9d). We find that equation (13) characterizes the data for $h/D_t > 0.5$ using $C_{L,sub} = 0.7$ and $C_{L,sub} = 1$ for supercritical and subcritical flows, respectively. For $h/D_t < 0.5$, lift coefficients become increasingly negative and are not well represented by equation (13). Again, the lift coefficients by definition already account for the added buoyant weight of the particle as it becomes partially submerged; effective lift coefficients that do not account for the change in buoyant particle weight with particle submergence (open symbols in Figure 9) are much more negative. Thus, the negative lift coefficients given by the filled symbols in Figures 9b and 9d indicate a hydraulic force acting on the particles directed into the bed.

4.4. Fluctuating Forces

The fluctuating forces, represented by the standard deviation of the force time series, in both lift and drag scale linearly with the $\rho U_{surf}^2 A_{sub}$ (Figure 10). The trend exists across the entire range of channel slopes and Froude numbers and appears to be independent of relative submergence for $h/D_t > 0.5$. For $h/D_t < 0.5$, the data are scattered, which may reflect uncertainty in calculating the appropriate portion of the upstream-facing particle area due to the detached and complex spray over the particle top (Figure 4). In addition, data scatter near 0.1 N is expected due to the instrument accuracy. The bulk of the data for $h/D_t > 0.5$ match what is expected from *Lamb et al.* [2008, 2017] that near-bed velocity fluctuations (σ_u) scale linearly with the depth-averaged velocity and produce force fluctuations that act on the particle.

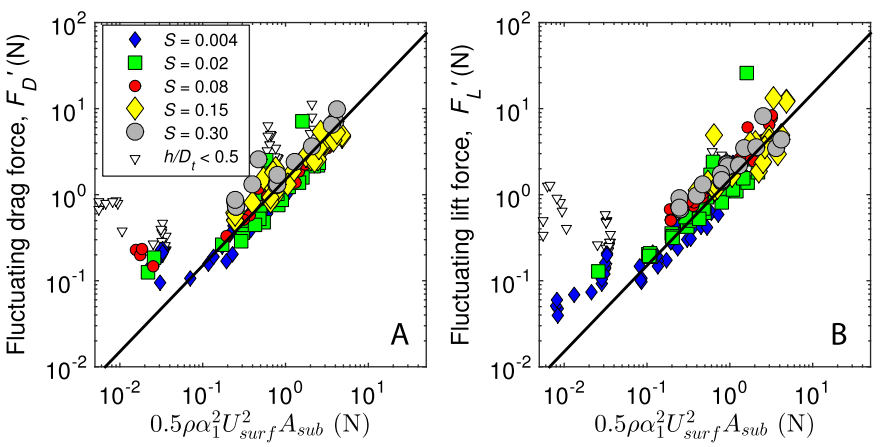

Figure 10. Standard deviation of (a) drag and (b) lift forces for all experiments. The solid line is equation (11) with $C_L' = C_D' = 1.5$. Instrument error is estimated at 0.1 N.

The fluctuating lift and drag coefficients (C_D' and C_L') needed to match the data are ~1.5 in both lift and drag.

5. Discussion

5.1. Lift and Drag Coefficients

For fully submerged particles, we find drag coefficients range from about 0.4 to 0.7 similar to previous studies of deep flow over a gravel bed [*Schmeeckle et al*., 2007], with the higher end of the range in our experiments corresponding to subcritical Froude numbers. Our particle Reynolds numbers are larger than explored in most previous studies; however, we see no apparent trend with particle Reynolds number despite crossing the values typical of the drag crisis for free-stream particles [*Schlichting*, 1979], which might be due to wake interactions with the rough bed that prevented changes in C_D at these Reynolds numbers. Similar to *Schmeeckle et al*. [2007], the largest effect on C_D for fully submerged particles is from the particle size relative to the bed roughness scale ($D_t/D_{50\text{-}bed}$). Larger particles are more exposed to the flow, and likely able to develop a more substantial wake zone without interference from the upstream or downstream particles, resulting in larger drag coefficients similar to free-stream values. Particles of similar size as the bed sediment sat within a pocket between neighboring particles and C_D was approximately a factor of five smaller (Figure 7). We also find that the lift coefficients are highly scattered with no clear relationship with $D_t/D_{50\text{-}bed}$, similar to findings of *Schmeeckle et al*. [2007], possibly due to changes in the orientation of the wake at the downstream end of the particle, as they discussed.

Our experiments revealed major changes in the drag and lift coefficients for shallow flows. Drag coefficients systematically increase as the flow shallowed for partially emerged particles ($h/D_t < 1$), consistent with the experiments of *Flammer et al*. [1970] for a hemisphere test particle over a smooth bed. We interpret the larger drag coefficients to be due to more tortuous water flow paths deeper within the grain roughness layer for $h/D_t < 1$. We also interpret the peak in C_D in Figure 9b for partially submerged particles with low Froude numbers and $0.5 < h/D_t < \sim 1$ to be a result of the standing waves evident in Figures 3e and 4a. The pileup of water on the upstream side of the particle and the water surface depression at the lee of the particle should result in additional downstream directed pressure force. Similar phenomena have been documented before and coined *wave drag* [*Flammer et al*., 1970]. Consistent with this hypothesis, the amplitude of the wave was larger at $S = 0.02$ (Figure 4a) as compared with $S = 0.004$ (Figure 3e), which explains why the peak in C_D was also larger for the steeper case (Figure 9c). *Flammer et al*. found that wave drag was a function of Fr with a peak in C_D at Fr = 0.6. Our results also show larger C_D for Fr ~ 0.6, at least for $h/D_t < \sim 1$ (Figure 8a).

To our knowledge, previous workers have not measured directly lift forces as a function of relative particle submergence. Our experiments show that C_L decreases from approximately 0.7 to zero as h/D_t goes from ~5 to unity, and surprisingly is strongly negative for $h/D_t < 1$. The lift force might be interpreted in terms of the Bernoulli effect in which faster flow below the particle, compared with flow above it, produces negative lift for shallowly submerged particles. Although the zone of subsurface flow was only approximately half a grain diameter thick, subsurface flow velocities were high on steep slopes, due to the lack of fines in the experiments. Nonetheless, subsurface flow velocities were always substantially slower than surface flow velocities (Figure 5a). Importantly, we also observed negative lift forces in experiments with low bed gradients (e.g., $S = 0.004$; Figure 9d) for which subsurface flows were negligible [*Lamb et al*., 2017]. Therefore, instead of a Bernoulli effect associated with the permeable bed, we interpret the reduction of lift with decreasing h/D_t to reflect spilling flow that directs the wake at the lee of the particle downward into the bed (Figures 3 and 4). In deep flow, the wake may have an orientation slightly upward, producing positive lift [*Schmeeckle et al*., 2007]. As the flow depth decreases, the wake orientation is forced into a downstream direction, and as the water surface drops below height of the particle, spilling flow over the particle top may direct the wake obliquely into the bed (Figure 4a) creating a negative lift force.

For many of our experiments with $h/D_t < 1$, the particles were visually submerged with a shallow flow extending up and over the top of the particle. Despite the complex water surface over the particle top, and its changing character with Froude number (Figure 4), the average flow depth in the test section, rather

than the local flow depth, characterized well the onset of heightened C_D and the change in sign of C_L at $h/D_t = 1$. This finding supports our assumption that particle buoyancy for partially emerged particles is a function of the average flow depth, rather than the local flow depth. It is likely that this thin sheet of spilling or shooting, detached flow over the particle top does not contribute to the hydrostatic component of pressure acting on the submerged portion of the particle.

Our results confirm that velocity fluctuations due to turbulence cause fluctuations in lift and drag forces acting on particles that scale linearly with the square of the depth-averaged velocity and that $C'_D \approx C'_L \approx 1.5$. The normalized fluctuating forces are remarkably insensitive to bed slope, Froude number, relative particle size ($D_t/D_{50\text{-}bed}$), and relative roughness for $h/D_t > 0.5$. *Lamb et al.* [2008] explained the dependence of near-bed turbulence on relative roughness as a result of depth-scale eddies with velocities that correlate with the depth-averaged flow rather than the local flow [see also *Nowell and Church*, 1979; *Recking et al.*, 2008a].

5.2. Implication for Friction Factors and Grain Drag

Large friction factors, C_f, are observed in steep mountain streams and often this is attributed to form drag from channel forms, such as step-pool sequences, or immobile boulders [*Buffington and Montgomery*, 1999; *Millar*, 1999; *Wilcox et al.*, 2006; *Yager et al.*, 2007; *Nitsche et al.*, 2011; *Ferguson*, 2012; *Schneider et al.*, 2015]. However, as discussed in section 1, heightened C_f might be explained by grain drag alone for flows with high relative roughness. Our direct measurements of grain drag allow for an estimation of the friction factor for flows of high relative roughness under the assumption that flow resistance is due to grain drag alone, and that the drag force measured on the test particle is representative of the bed sediment, which is true for the natural cobbles and an approximation for the spheres. Assuming a local momentum balance between the average boundary shear stress acting on the bed and resisting drag force on the particle, we find

$$\rho_w u_*^2 A_{plan} \approx \overline{F_D} = \frac{1}{2}\rho_w C_D \langle \bar{u} \rangle^2 A_{sub} \tag{14}$$

where A_{plan} is the bed surface area covered by the particle. Rearranging equation (14) and using the definition of C_f, we find that

$$C_f = \frac{1}{2} C_D \frac{A_{sub}}{A_{plan}} \frac{\langle \bar{u} \rangle^2}{U_{surf}^2} \tag{15}$$

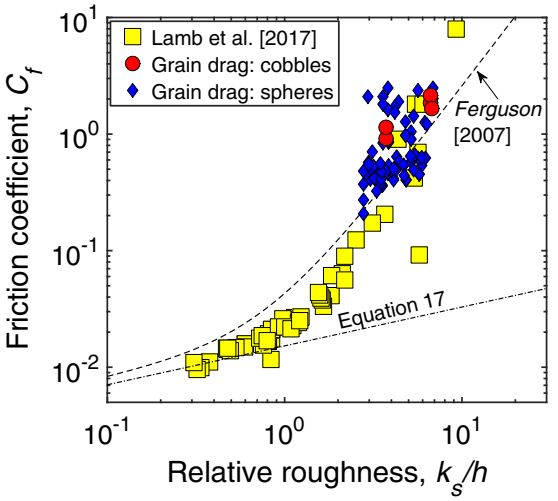

Figure 11. Bulk friction coefficient of the flow as a function of relative roughness calculated from measurements of the depth-averaged flow velocity by *Lamb et al.* [2017]. Also shown are our estimates of the bulk friction coefficient inferred from measurements of grain drag alone (equation (16)). Equation (17) represents a typical flow resistance relation developed for low-gradient rivers, and the empirical relation of *Ferguson* [2007] matches well with observations of flow resistance in mountain streams.

For the case of $h < D$, the velocity averaged over the particle cross section is approximately equivalent to the depth average velocity when adjusted by porosity in the roughness layer (ϕ_r), that is $\phi_r \langle \bar{u} \rangle \approx U_{surf}$. In addition, for spherical particles in which $h > 0.5D$, we approximate $A_{plan} \approx A$. Under these assumptions, equation (15) becomes

$$C_f = \frac{1}{2} C_D \frac{A_{sub}}{A} \frac{1}{\phi_r^2} \tag{16}$$

We calculated the expected friction factor, C_f, from equation (16) using our measured values of C_D for experiments with $0.5 < h/D_t < 1$ as a function of relative roughness (k_s/h) by setting $k_s = 2.5D_t$ and $\phi_r = 0.7$ [*Lamb et al.*, 2017]. Figure 11 shows that the expected bulk friction factors due to grain drag alone are large for shallowly submerged flow, with most estimates ranging between C_f of 0.5 and 2. These estimates are significantly larger than expected from relations developed for grain drag in low

gradient rivers, which are often applied to steep mountain streams, such as

$$C_f = a\left(\frac{h}{k_s}\right)^b \tag{17}$$

in which $a = 8.1$ and $b = -1/3$ are commonly used [*Parker*, 1991; *Rickenmann and Recking*, 2011]. Also shown in Figure 11 are the measured values of C_f from our companion experiments using the depth-averaged velocity as reported in *Lamb et al.* [2017], and the empirical relation of *Ferguson* [2007] that has been shown to be a good predictor of C_f for natural mountain streams that contain step-pool bed forms and other complex bed geometries [*Rickenmann and Recking*, 2011]. The overlap with our estimates of C_f from the direct force measurements and flow resistance measurements by *Lamb et al.* [2017] confirm our interpretation that flow resistance in these experiments is a result of grain drag alone. Moreover, the overlap in our measurements with the relationship of *Ferguson* [2007] suggests that grain drag can account for much of the high flow resistance observed in mountain streams, and that resistance equations developed for lowland rivers, like equation (17), substantially underestimate resistance due to grain drag in rivers with high relative roughness. These ideas also are consistent with the steep flume experiments of *Zimmermann* [2010] who found that C_f was approximately the same in cases with planar, gravel beds as compared with those with step-pool bed forms.

In addition to bed forms and channel forms, natural mountain streams also have a mixture of sediment sizes in the bed and bed load transport, all of which will tend to increase flow resistance, and thus their absence in our experiments cannot explain the observed high flow resistance. For example, bed load transport increases flow resistance on planar beds [*Wiberg and Rubin*, 1989; *Recking et al.*, 2008b], and fines would reduce subsurface flow velocities, which in turn would reduce surface flow velocities (equation (6)) and increase flow resistance [*Lamb et al.*, 2017]. Instead of these effects, we interpret the heightened values of C_f with increasing relative roughness as a result of (1) relatively slow flow within the roughness layer and (2) a roughness layer making up an increasing fraction of the total flow depth as relative roughness increases. We find, in addition, that for partially submerged particles, larger grain drag coefficients, C_D, are associated with large relative roughness (Figure 9), and this may explain why C_f continues to increase with relative roughness in cases where the roughness layer makes up the entire flow depth (Figure 11). We interpret heightened C_D for shallowly submerged particles to be caused by more tortuous flow paths deeper in the grain layer. As the flow shallows to the point of zero surface flow, flow resistance should increase further and eventually conform to that for subsurface flow alone, such as predicted using Darcy's law or equation (7).

Although grain drag may explain much of the heightened flow resistance observed in steep mountain streams, our experiments also support the idea that large isolated boulders can produce a disproportionate amount of momentum loss to the flow [*Yager et al.*, 2007]. However, the effect appears to be most pronounced for low gradient channels. For our experiments with $S = 0.004$, enhanced drag due to surface wave effects resulted in approximately a factor of 2 increase in C_D for grains with $h/D_t \sim 0.7$. In such low gradient channels, shallowly submerged particles with $h/D_t \sim 0.7$ are unlikely to be transported [e.g., *Lamb et al.*, 2008]. Still, these large immobile boulders produce a drag force on the flow per unit bed area that would be several fold larger than that of smaller sediment because of higher C_D due to wave drag and large $D_t/D_{50\text{-}bed}$, in addition to accessing faster flow higher above the bed.

5.3. Implications for Sediment Transport

Sediment transport relations often assume that the average boundary shear stress, τ_b, is a good representation of the hydraulic drag force on bed sediment, per unit bed area, and that the drag force in turn scales linearly with the lift force (i.e., $\tau_b A \propto F_D \propto F_L$). For example, this assumption is the basis of the Shields number, τ_*, used to characterize initial sediment motion and the sediment flux [*Shields*, 1936; *Meyer-Peter and Müller*, 1948]. We can test the assumption that $\tau_b A \propto F_D \propto F_L$ directly with our force-balance measurements by computing a normalized particle drag force, $F_D/(\tau_b A)$, and normalized lift force, $F_L/(\tau_b A)$. Note that these normalized forces differ from the drag and lift coefficients because the normalization uses the boundary shear stress and the total particle cross-sectional area, rather than the local flow velocity and the submerged cross-sectional area. Thus, following equation (2), the normalized forces account for both the drag (or lift)

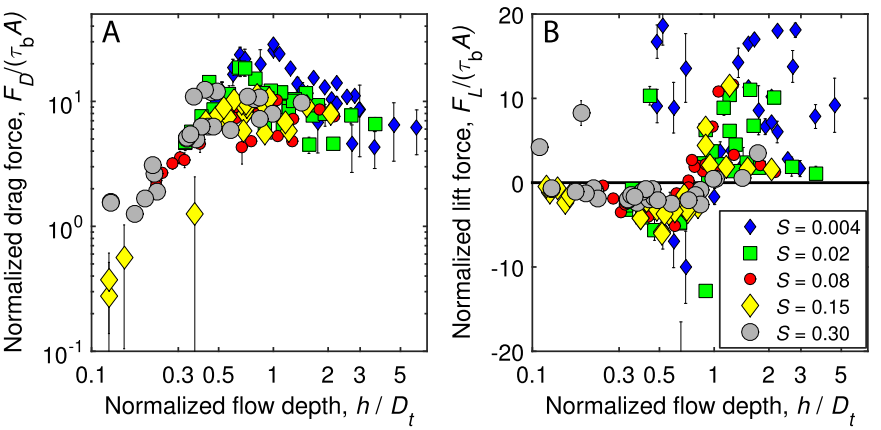

Figure 12. Normalized (a) drag and (b) lift forces (see equation (2)) as a function of relative particle submergence. All data are shown. Error bars represent instrument error of 0.3 N.

coefficient and the local velocity profile ($\langle \bar{u} \rangle / u_*$) and are a useful metric to analyze if hydraulic forces on particles scale with the boundary shear stress or Shields number.

Figure 12a shows that the normalized drag force, $F_D/(\tau_b A)$, is approximately constant for all particles with $h/D_t > 0.5$ regardless of channel slope, thus largely verifying the Shields' approach for drag. For the lowest gradient experiments ($S = 0.004$), normalized drag forces were significantly larger for $h/D_t \sim 1$, which we interpret as resulting from wave drag effects as discussed in section 5.1. Although C_D increases with particle emergence ($h/D_t < 1$ in Figures 9a and 9b), the normalized drag force drops rapidly for $h/D_t < 0.5$. Thus, while very shallow flows have high drag coefficients (Figure 9), these high coefficients are outweighed by slower local flow velocities deeper within the grain roughness layer, and the smaller particle area over which the force is applied for partially emerged particles, resulting in a rapid reduction in the normalized drag force for $h/D_t < 0.5$.

The normalized lift force is scattered for fully submerged particles, but in general is larger for deeper flow (Figure 12b). $F_L/(\tau_b A)$ is approximately zero for $h/D_t = 1$, negative for $h/D_t < 1$, and has a minimum (maximum negative lift) at $h/D_t \sim 0.5$. These trends are largely dictated by the lift coefficient (Figures 9b and 9c). For $h/D_t < 0.5$, the normalized lift force, like the normalized drag force, tends to zero primarily because the submerged, upstream-facing cross-sectional area of the particle is small.

Together, the results shown in Figure 12 suggest that heightened critical Shields numbers in steep rivers with high relative roughness are not the result of changes in drag forces on particles, counter to assumptions in previous models [*Lamb et al*., 2008; *Recking*, 2009; *Ferguson*, 2012]. Instead, as long as $h/D > 0.5$, which is typically the case in natural streams capable of transporting bed sediment, the drag force should scale approximately linearly with the average boundary shear stress. Instead of drag, it is the normalized lift force that changes significantly as a function of relative roughness. Although the lift force is often assumed to scale linearly with the drag force and boundary shear stress [*Wiberg and Smith*, 1987; *James*, 1990; *Lamb et al*., 2008], this clearly is not the case for shallowly submerged particles. Streams with steeper bed slopes necessarily have lower particle submergence at conditions of initial sediment motion [*Prancevic and Lamb*, 2015a]; therefore, the lower, and even negative, lift forces associated with shallow flows would produce more stable sediment, higher critical Shields numbers and lower sediment fluxes.

To explore the effect of reduced lift forces on sediment transport in steep streams, here we modify the force-balance model of *Lamb et al*. [2008] to calculate the critical Shields number for initial sediment motion. In addition to changes in lift force, steep streams with high relative roughness also should have lower fluctuations in the lift and drag forces due to the reduced intensity of turbulence, following equation (11), which also effects sediment transport. *Lamb et al*. [2008], following *Wiberg and Smith* [1985], balanced lift, drag, buoyancy, and gravitational forces on a particle to derive the critical Shields number:

$$\tau_{*c}=\frac{2}{C_D}\frac{u_*^2}{\langle u^2\rangle}\frac{1}{f_{gd}}\left(\frac{\tan\phi_0-\tan\theta}{1+(F_L/F_D)\tan\phi_0}\right)\left[\frac{V}{A_{sub}D}\frac{1}{r}\left(\frac{\rho_s}{\rho_w}-\frac{V_{sub}}{V}\right)\right] \quad (18)$$

in which $f_{gd}=(\tau_T-\tau_m)/\tau_T$ is the fraction of the total stress, $\tau_T \approx \rho g h \sin\theta$, spent on grain drag rather than morphologic form drag (τ_m); ϕ_0 is the sediment friction angle; and $r=(\rho_s-\rho_w)/\rho_w$ is the submerged specific density of sediment. The bracketed term accounts for reduced buoyancy for particles that are partially emerged from the flow. Following *Lamb et al*. [2008], we set $\rho_s = 2650$ kg/m^3, and $\rho_w = 1000$ kg/m^3, and explore $\phi_0 = 52°$ typical of natural gravel in flume experiments and $\phi_0 = 68°$ for natural mountain streams [*Prancevic and Lamb*, 2015b].

For $\langle u\rangle/u_*$, we use the velocity model given by equation (6), which does not depend on bed slope or relative roughness for cases with negligible subsurface flow ($u_0 = 0$). Following *Lamb et al*. [2008], we assume that particle transport occurs under the vector sum of the local time-averaged flow and downstream velocity excursions due to turbulence, so that

$$u^2 \approx \overline{u^2}+\sigma_u^2 \quad (20)$$

and we determine σ_u from equation (3). Finally, we incorporate our new relations for the lift and drag coefficients using equations (12) and (13) for subcritical flow.

The resulting model produces an increasing critical Shields stress at initial sediment motion with increasing channel slope (Figure 13). For $S < 0.01$, the model predicts that the critical Shields stress increases with channel slope primarily because of the effect of reduced turbulence intensities on steeper slopes with higher relative roughness. For $0.01 < S < 0.3$, τ_{*c} increases more rapidly with increasing channel slope because of the reduced or negative lift forces, in addition to further reduction in turbulence intensities. Finally, for $S > 0.3$, reduced buoyancy due to particle emergence produces even larger τ_{*c} until the bed slopes reach the stability criteria for *en masse* failure [*Prancevic et al*., 2014].

The force-balance model predictions match well the trend of the data compilation from field observations and flume experiments, and the magnitude is similar to observations from planar beds that lacked morphologic form drag [e.g., *Prancevic et al*., 2014]. Much of the field data plot above the baseline ($f_{gd} = 1$) predictions and can be better described by applying a constant morphologic form-drag correction to all the data of $f_{gd} = 0.5$ (Figure 13). Thus, while an increasing fraction of morphologic form drag in steeper streams does not appear to be needed to explain the trend of τ_{*c} with channel slope, a constant fraction of morphologic form drag applied equally to all bed slopes does allow the model to better fit the field data. Note that while the models proposed by *Lamb et al*. [2008], *Recking* [2009], and *Ferguson* [2012] also matched similar data

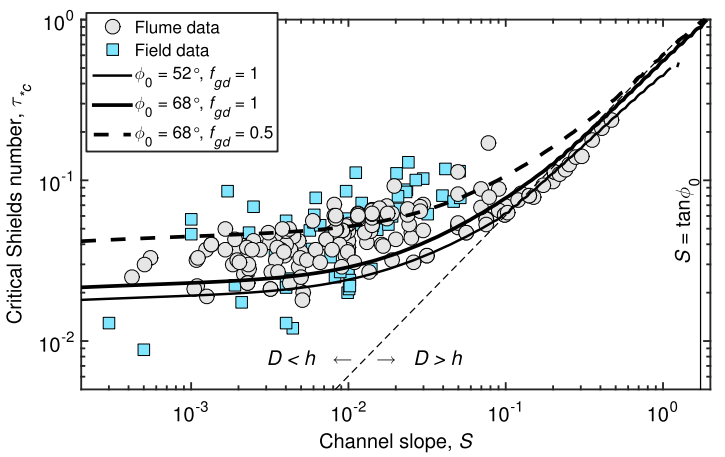

Figure 13. Critical Shields number for incipient sediment motion modeled using equation (18) and our new relations for the lift and drag coefficients. Three versions of the model are shown corresponding to conditions typical of laboratory gravel ($\phi_0 = 52°$, $f_{gd} = 100\%$), natural steep streams ($\phi_0 = 68°$ [*Prancevic and Lamb*, 2015b] assuming no morphologic form drag, $f_{gd} = 100\%$), and $\phi_0 = 68°$ and $f_{gd} = 50\%$. All calculations use $C_{L,sub} = 1$ and $C_{D,sub} = 0.4$ corresponding to subcritical flow, consistent with the calculation for all but the steepest slopes ($S > 0.3$). The data compilation of field and laboratory data comes from previous compilations of *Lamb et al*. [2008] and *Prancevic et al*. [2014].

compilations, their models required unverified assumptions that near-bed flow velocities decrease with increasing relative roughness and that the drag and lift coefficients are constants. Our results instead show that near-bed flow velocities and drag forces are approximately invariant with relative roughness, and that the increase in τ_{*c} with bed slope is due to reductions in the lift force and turbulence intensity with higher relative roughness. This analysis also is consistent with experiments that show that much of the increase in τ_{*c} with bed slope can be reproduced in experiments with planar gravel beds that lacked bed forms and other sources of morphologic form drag [*Prancevic et al*., 2014].

Because relationships for bed load flux, q_b, are typically a function of the difference between the Shields number and the critical Shields number [*Meyer-Peter and Müller*, 1948], i.e.,

$$q_b \propto (\tau_* - \tau_{*c})^{3/2} \tag{21}$$

a larger τ_{*c} will also result in a smaller sediment flux in steep rivers with high relative roughness. Indeed, *Schneider et al*. [2015] showed that bed load flux data from steep mountain streams can be adequately explained by using either a heightened critical Shields number, τ_{*c}, or a morphologic form-drag correction applied to τ_* that increases with channel slope. They were unable to decipher which approach is correct from field data comparisons alone. Our direct measurements of large flow resistance, C_f, from grain drag in experiments that lacked channel forms and bed forms suggest that morphologic form drag is not as large as often assumed in stress-partitioning approaches [*Lamb et al*., 2017]. Instead, we suggest that sediment fluxes are lower than expected in steep streams, as compared with low gradient rivers, for the same reasons that the critical Shields stresses are larger than expected—reduced turbulent intensities and reduced lift forces associated with high relative roughness. In addition, lift and drag forces control particle trajectories [*Wiberg and Smith*, 1985]; in steep and shallow flows with reduced lift forces, bed load particles might have shorter hop lengths, slower transport velocities, and tend to roll more than saltate, which should also reduce bed load fluxes.

6. Conclusions

We report on direct measurements of lift and drag forces on near-bed cobbles over a rough, planar bed across a wide range of bed slopes ($0.004 < S < 0.3$) and flow discharges. For fully submerged particles, lift coefficients were highly variable whereas drag coefficients were primarily a function of the test particle size, D_t, relative to the grain sizes on the bed. Larger particles were more exposed to the flow, and had larger drag coefficients of $C_D \sim 0.7$, whereas particles that sat in pockets between neighboring particles had smaller drag forces with $C_D \sim 0.1$. As the flow depth, h, shallowed relative to the particle size, lift coefficients systematically dropped, were near zero for particles that were just submerged, and became increasingly negative for partially submerged particles, indicating a significant hydraulic force that pulls particles toward the bed. In contrast, drag coefficients for partially submerged particles increased and exceeded unity for $h/D_t < 0.5$. Drag coefficients were also a function of Froude number, Fr, with larger C_D observed for subcritical Froude numbers, and a peak in C_D for $h/D_t \sim 0.6$ possibly due to surface wave effects. Fluctuations in the lift and drag forces due to turbulence scale similarly with the square of the depth-averaged flow velocity, in contrast to the common assumption of a bed shear-velocity scaling relation.

Together these results have implications for our understanding of flow resistance and sediment transport in steep rivers. The direct measurements of large drag coefficients in shallow flows confirm the results within our companion paper [*Lamb et al*., 2017] that flow resistance due to grain drag alone can be large in flows with high relative roughness and can explain observations of high flow resistance in steep mountain streams without the need to invoke heightened morphologic form drag from bed forms and channel forms. Thus, stress-partitioning approaches commonly used to calculate sediment transport in steep mountain rivers may be overestimating the role of morphologic form drag from complex bed topography.

Instead of morphologic form drag, our results suggest that heightened stability of sediment and lower-than-expected sediment fluxes in steep mountain streams are due to changes in the lift force and turbulent fluctuations acting on bed sediment. Our measurements show that lift forces on particles decrease significantly with increasing relative roughness, becoming negative for partially submerged particles. Using a model, we show that this reduction in lift, combined with reduced near-bed turbulence intensity, can explain the observed increase in critical Shields stress for incipient sediment motion with increasing

channel-bed slope in the absence of complex bed topography. Because bed load flux relations are functions of the critical Shields number, reduced lift forces and reduced turbulence intensities might also explain observations of lower-than-expected bed load fluxes in steep mountain rivers.

Acknowledgments
Emilio Graff built the force balance and helped with instrument calibration. We thank Florent Gimbert for help interpreting Figure 2b. Funding was provided by the National Science Foundation grants EAR-0922199 and EAR-1349115, and the Caltech Terrestrial Hazard Observation and Reporting program. Thanks to Paul Carling, Mário Franca, and two anonymous reviewers for their useful critiques. Experimental data can be found in the supporting information.

References

Aberle, J., and G. M. Smart (2003), The influence of roughness structure on flow resistance on steep slopes, *J. Hydraul. Res.*, *41*(3), 259–269.
Aivazyan, O. M. (1987), Stabilized aeration on chutes, *Hydrotech. Construct.*, *20*, 713–722, doi:10.1007/BF01425070.
Bagnold, R. A. (1974), Fluid forces on a body in shear-flow—Experimental use of stationary flow, *Proc. R. Soc. London, Ser. A*, *340*(1621), 147–171, doi:10.1098/rspa.1974.0145.
Bathurst, J. C. (1985), Flow resistance estimation in mountain rivers, *J. Hydraul. Eng.*, *111*(4), 625–643.
Bathurst, J. C. (2002), At-a-site variation and minimum flow resistance for mountain rivers, *J. Hydrol.*, *269*(1–2), 11–26, doi:10.1016/S0022-1694(02)00191-9.
Bathurst, J. C., R. M. Li, and D. B. Simons (1981), Resistance equation for large-scale roughness, *J. Hydraul. Div. Am. Soc. Civ. Eng.*, *107*(12), 1593–1613.
Bernhardt, E. S., et al. (2005), Ecology—Synthesizing us river restoration efforts, *Science*, *308*(5722), 636–637.
Buffington, J. M., and D. R. Montgomery (1999), Effects of hydraulic roughness on surface textures of gravel-bed rivers, *Water Resour. Res.*, *35*(11), 3507–3521, doi:10.1029/1999WR900138.
Buffington, J. M., D. R. Montgomery, and H. M. Greenberg (2004), Basin-scale availability of salmonid spawning gravel as influenced by channel type and hydraulic roughness in mountain catchments, *Can. J. Fish. Aquat. Sci.*, *61*(11), 2085–2096, doi:10.1139/f04-141.
Cao, H. H. (1985), *Resistance hydraulique d'un lit à gravier mobile à pente raide; étude expérimentale*, 285 pp., Ecole Polytech. Fed. de Lausane, Lausanne, Switzerland.
Carling, P. A., M. Hoffmann, A. A. Blatter, and A. Dittrich (2002), Drag of emergent and submerged rectangular obstacles in turbulent flow above bedrock surface, in *Rock Scour due to Falling High-Velocity Jets*, edited by A. J. Schleiss and E. Bollaert, pp. 83–94, Swets and Zeitlinger, Lisse, Netherlands.
Carollo, F. G., V. Ferro, and D. Termini (2005), Analyzing turbulence intensity in gravel bed channels, *J. Hydraul. Eng.*, *131*(12), 1050–1061, doi:10.1061/(ASCE)0733-9429(2005)131:12(1050).
Chanson, H. (1994), Air-water-interface area in self-aerated flows, *Water Res.*, *28*(4), 923–929, doi:10.1016/0043-1354(94)90100-7.
Chaplin, J. R., and P. Teigen (2003), Steady flow past a vertical surface-piercing circular cylinder, *J. Fluids Struct.*, *18*(3–4), 271–285, doi:10.1016/j.jfluidstructs.2003.07.009.
Cheng, E. D. H., and C. G. Clyde (1972), Instantaneous hydrodynamic lift and drag forces on large roughness elements in turbulent open channel flow, in *Sedimentation, Symposium to Honor Professor H.A. Einstein*, edited by H. S. Shen, pp. 3.1–3.20, Colo. State Univ., Fort Collins, Colo.
Chepil, W. S. (1958), The use of evenly spaced hemispheres to evaluate aerodynamic forces on a soil surface, *Trans. AGU*, *39*(3), 397–404.
Chiew, Y., and G. Parker (1995), Reply to "incipient motion on nonhorizontal slopes," *J. Hydraul. Res.*, *33*(5), 728–730.
Christensen, B. A. (1972), Incipient motion on cohesionless channel banks, in *Sedimentation, Symposium to Honor Professor H.A. Einstein*, edited by H. S. Shen, pp. 1–22, Colo. State Univ., Fort Collins.
Christensen, B. A. (1995), Discussion of "incipient motion on nonhorizontal slopes," *J. Hydraul. Res.*, *33*(5), 725–728.
Dittrich, A., and K. Koll (1997), Velocity field and resistance of flow over rough surfaces with large and small relative roughness, *Int. J. Sediment Res.*, *12*(3), 21–33.
Dwivedi, A., B. Melville, and A. Y. Shamseldin (2010), Hydrodynamic forces generated on a spherical sediment particle during entrainment, *J. Hydraul. Eng.*, *136*(10), 756–769, doi:10.1061/(ASCE)HY.1943-7900.0000247.
Dwivedi, A., B. W. Melville, A. Y. Shamseldin, and T. K. Guha (2011), Analysis of hydrodynamic lift on a bed sediment particle, *J. Geophys. Res.*, *116*, F02015, doi:10.1029/2009JF001584.
Einstein, H. A., and E. A. El-Samni (1949), Hydrodynamic forces on a rough wall, *Rev. Mod. Phys.*, *21*(3), 520–524, doi:10.1103/RevModPhys.21.520.
Ferguson, R. I. (2012), River channel slope, flow resistance, and gravel entrainment thresholds, *Water Resour. Res.*, *48*, W05517, doi:10.1029/2011WR010850.
Ferguson, R. (2007), Flow resistance equations for gravel- and boulder-bed streams, *Water Resour. Res.*, *43*, W05427, doi:10.1029/2006WR005422.
Ferro, V. (2003), Flow resistance in gravel-bed channels with large-scale roughness, *Earth Surf. Processes Landforms*, *28*(12), 1325–1339, doi:10.1002/esp.589.
Flammer, G. H., J. P. Tullis, and E. S. Mason (1970), Free surface, velocity gradient flow past hemisphere, *J. Hydraul. Div. Am. Soc. Civ. Eng.*, *7*, 1485–1502.
Ghisalberti, M. (2009), Obstructed shear flows: Similarities across systems and scales, *J. Fluid Mech.*, *641*, 51–61, doi:10.1017/S0022112009992175.
Gimbert, F., V. C. Tsai, and M. P. Lamb (2014), A physical model for seismic noise generation by turbulent flow in rivers, *J. Geophys. Res. Earth Surf.*, *119*, 2209–2238, doi:10.1002/2014JF003201.
Hay, A. D. (1947), Flow about semi-submerged cylinders of finite length, report, 174 pp., Princeton Univ., Princeton, N. J.
James, C. S. (1990), Prediction of entrainment conditions for nonuniform, noncohesive sediments, *J. Hydraul. Res.*, *28*(1), 25–41.
Kamphuis, J. W. (1974), Determination of sand roughness for fixed beds, *J. Hydraul. Res.*, *12*(2), 193–202.
Lamb, M. P., W. E. Dietrich, and J. G. Venditti (2008), Is the critical Shields stress for incipient sediment motion dependent on channel-bed slope?, *J. Geophys. Res.*, *113*, F02008, doi:10.1029/2007JF000831.
Lamb, M. P., F. Brun, and B. M. Fuller (2017), Hydrodynamics of steep streams with planar coarse-grained beds: Turbulence, flow resistance, and implications for sediment transport, *Water Resour. Res.*, *53*, 2240–2263, doi:10.1002/2016WR019579.
Lawrence, D. S. L. (2000), Hydraulic resistance in overland flow during partial and marginal surface inundation: Experimental observations and modeling, *Water Resour. Res.*, *36*(8), 2381–2393.
Lee, H., and S. Balachandar (2012), Critical shear stress for incipient motion of a particle on a rough bed, *J. Geophys. Res.*, *117*, F01026, doi:10.1029/2011JF002208.
Lee, H., and S. Balachandar (2017), Effects of wall roughness on drag and lift forces of a particle at finite Reynolds number, *Int. J. Multiphase Flow*, *88*, 116–132, doi:10.1016/j.ijmultiphaseflow.2016.09.006.

Lenzi, M. A., V. D'Agostino, and P. Billi (1999), Bedload transport in the instrumented catchment of the Rio Cordon. Part 1: Analysis of bed-load records, conditions and threshold of bedload movement, *Catena*, *36*, 171–190.
Meyer-Peter, E., and R. Müller (1948), Formulas for bed-load transport, in *Proceedings of the 2nd Congress, International Association of Hydraulic Research*, pp. 39–64, Int. Assoc. of Hydraul. Res., Stockholm.
Millar, R. G. (1999), Grain and form resistance in gravel-bed rivers, *J. Hydraul. Res.*, *37*(3), 303–312.
Mizuyama, T. (1977), Bedload transport in steep channels, PhD dissertation, 118 pp., Kyoto Univ., Kyoto, Japan.
Mueller, E. R., J. Pitlick, and J. Nelson (2005), Variation in the reference Shields stress for bed load transport in gravel-bed streams and rivers, *Water Resour. Res.*, *41*, W04006, doi:10.1029/2004WRR003692.
Nepf, H. M., and E. R. Vivoni (2000), Flow structure in depth-limited, vegetated flow, *J. Geophys. Res.*, *105*(C12), 28,547–28,557, doi:10.1029/2000JC900145.
Nezu, I., and H. Nakagawa (1993), *Turbulence in Open-Channel Flows*, 281 pp., A. A. Balkema, Rotterdam, Netherlands.
Nikora, V., D. Goring, I. McEwan, and G. Griffiths (2001), Spatially averaged open-channel flow over rough bed, *J. Hydraul. Eng.*, *127*(2), 123–133.
Nitsche, M., D. Rickenmann, J. M. Turowski, A. Badoux, and J. W. Kirchner (2011), Evaluation of bedload transport predictions using flow resistance equations to account for macro-roughness in steep mountain streams, *Water Resour. Res.*, *47*, W08513, doi:10.1029/2011WR010645.
Novak, P., and C. Nalluri (1984), Incipient motion of sediment particles over fixed-beds, *J. Hydraul. Res.*, *22*(3), 181–197.
Nowell, A. R. M., and M. Church (1979), Turbulent flow in a depth-limited boundary layer, *J. Geophys. Res.*, *88*(C8), 4816–4824.
Parker, G. (1991), Selective sorting and abrasion of river gravel. I: Applications, *J. Hydraul. Eng.*, *117*(2), 150–171.
Prancevic, J. P., and M. P. Lamb (2015a), Unraveling bed slope from relative roughness in initial sediment motion, *J. Geophys. Res. Earth Surf.*, *120*, 474–489, doi:10.1002/2014JF003323.
Prancevic, J. P., and M. P. Lamb (2015b), Particle friction angles in steep mountain channels, *J. Geophys. Res. Earth Surf.*, *120*, 242–259, doi:10.1002/2014JF003286.
Prancevic, J. P., M. P. Lamb, and B. M. Fuller (2014), Incipient sediment motion across the river to debris-flow transition, *Geology*, *42*(3), 191–194, doi:10.1130/G34927.1.
Recking, A. (2009), Theoretical development on the effects of changing flow hydraulics on incipient bed load motion, *Water Resour. Res.*, *45*, W04401, doi:10.1029/2008WR006826.
Recking, A., P. Frey, A. Paquier, P. Belleudy, and J. Y. Champagne (2008a), Feedback between bed load transport and flow resistance in gravel and cobble bed rivers, *Water Resour. Res.*, *44*, W05412, doi:10.1029/2007WR006219.
Recking, A., P. Frey, A. Paquier, P. Belleudy, and J. Y. Champagne (2008b), Bed-load transport flume experiments on steep slopes, *J. Hydraul. Eng.*, *134*(9), 1302–1310, doi:10.1061/(ASCE)0733-9429(2008)134:9(1302).
Rice, C. E., K. C. Kadavy, and K. M. Robinson (1998), Roughness of loose rock riprap on steep slopes, *J. Hydraul. Eng.*, *124*(2), 179–185, doi:10.1061/(ASCE)0733-9429(1998)124:2(179).
Rickenmann, D. (2001), Comparison of bed load transport in torrents and gravel bed streams, *Water Resour. Res.*, *37*(12), 3295–3305, doi:10.1029/2001WR000319.
Rickenmann, D. (2012), Alluvial steep channels: Flow resistance, bedload transport and transition to debris flows., in *Gravel Bed Rivers: Processes, Tools, Environment*, edited by M. Church, P. Biron, and A. Roy, pp. 386–397, John Wiley, Chichester, U. K.
Rickenmann, D., and A. Recking (2011), Evaluation of flow resistance in gravel-bed rivers through a large field data set, *Water Resour. Res.*, *47*, W07538, doi:10.1029/2010WR009793.
Roberson, J. A., and C. K. Chen (1970), Flow in conduits with low roughness concentration, *J. Hydraul. Div. Am. Soc. Civ. Eng.*, *96*, 941–957.
Scheingross, J. S., E. W. Winchell, M. P. Lamb, and W. E. Dietrich (2013), Influence of bed patchiness, slope, grain hiding, and form drag on gravel mobilization in very steep streams, *J. Geophys. Res. Earth Surf.*, *118*, 982–1001, doi:10.1002/jgrf.20067.
Schlichting, H. (1979), *Boundary-Layer Theory*, 7th ed., 535 pp., McGraw-Hill, New York.
Schmeeckle, M. W., and J. M. Nelson (2003), Direct numerical simulation of bedload transport using a local, dynamic boundary condition, *Sedimentology*, *50*(2), 279–301, doi:10.1046/j.1365-3091.2003.00555.x.
Schmeeckle, M. W., J. M. Nelson, and R. L. Shreve (2007), Forces on stationary particles in near-bed turbulent flows, *J. Geophys. Res.*, *112*, F02003, doi:10.1029/2006JF000536.
Schneider, J. M., D. Rickenmann, J. M. Turowski, K. Bunte, and J. W. Kirchner (2015), Applicability of bed load transport models for mixed-size sediments in steep streams considering macro-roughness, *Water Resour. Res.*, *51*, 5260–5283, doi:10.1002/2014WR016417.
Shields, A. (1936), Awendung der aehnlichkeitsmechanik und der turbulenzforschung auf die geschiebebewegung, *Mitt. Preuss. Versuch-sanst. Wasserbau Schiffbau*, 26, 26.
Straub, L. G., and O. P. Lamb (1956), Studies of air entrainment on open-channel flows, *Am. Soc. Civ. Eng. Trans.*, *121*, 30–44.
Tennekes, H., and J. L. Lumley (1972), *A First Course in Turbulence*, vol. xii, 300 pp., MIT Press, Cambridge, Mass.
Wang, J., C. K. Chen, Z. N. Dong, and X. Zhenhuan (1993), The effects of bed roughness on the distribution of turbulent intensities in open-channel flow, *J. Hydraul. Res.*, *31*(1), 89–98.
Wiberg, P. L., and D. M. Rubin (1989), Bed roughness produced by saltating sediment, *J. Geophys. Res.*, *94*(C4), 5011–5016, doi:10.1029/JC094iC04p05011.
Wiberg, P. L., and J. D. Smith (1985), A theoretical-model for saltating grains in water, *J. Geophys. Res.*, *90*(C4), 7341–7354, doi:10.1029/JC090iC04p07341.
Wiberg, P. L., and J. D. Smith (1987), Calculations of the critical shear stress for motion of uniform and heterogeneous sediments, *Water Resour. Res.*, *23*(8), 1471–1480.
Wiberg, P. L., and J. D. Smith (1991), Velocity distribution and bed roughness in high-gradient streams, *Water Resour. Res.*, *27*(5), 825–838.
Wilcox, A. C., J. M. Nelson, and E. E. Wohl (2006), Flow resistance dynamics in step-pool channels: 2. Partitioning between grain, spill, and woody debris resistance, *Water Resour. Res.*, *42*, W05419, doi:10.1029/2005WR004278.
Yager, E. M., J. W. Kirchner, and W. E. Dietrich (2007), Calculating bed load transport in steep boulder bed channels, *Water Resour. Res.*, *43*, W07418, doi:10.1029/2006WR005432.
Yager, E. M., W. E. Dietrich, J. W. Kirchner, and B. W. McArdell (2012), Prediction of sediment transport in step-pool channels, *Water Resour. Res.*, *48*, W01541, doi:10.1029/2011WR010829.
Zimmermann, A. (2010), Flow resistance in steep streams: An experimental study, *Water Resour. Res.*, *46*, W09536, doi:10.1029/2009WR007913.